

## Lamb shift and the lifetime of the $2^2S_{1/2}$ state of hydrogenlike argon ( $Z=18$ )

Harvey Gould

*Materials and Molecular Research Division, Building 71-259, Lawrence Berkeley Laboratory,  
University of California at Berkeley, Berkeley, California 94720*

Richard Marrus

*Materials and Molecular Research Division, Building 71-259, Lawrence Berkeley Laboratory,  
University of California at Berkeley, Berkeley, California 94720  
and Department of Physics, University of California at Berkeley, Berkeley, California 94720*

(Received 17 January 1983)

We report a measurement of the Lamb shift in hydrogenlike argon based on the electric-field-quenching method, and a measurement of the unperturbed lifetime of the  $2^2S_{1/2}$  state. We find the lifetime of the unperturbed  $2^2S_{1/2}$  state to be 3.487(0.036) ns in agreement with the theoretical value of 3.497 ns. This is the first measurement of the  $2^2S_{1/2}$  state lifetime of sufficient accuracy to observe the contribution to the total decay rate of the single-photon magnetic dipole decay. Our measured value of the Lamb shift is  $\delta E(2^2S_{1/2}-2^2P_{1/2})=37.89(0.38)$  THz, lower than, but in agreement with, Mohr's value of 38.25(0.025) THz, and 2.7 standard deviations below Erickson's value of 39.01(0.16) THz. Both the quenched and natural lifetimes were measured by the beam-foil time-of-flight technique. In this paper we emphasize the treatment of the systematic effects in the beam-foil time-of-flight method including cascades from higher excited states, interference from the spectra of heliumlike ions, collisions in the residual gas, and perturbations from a highly excited extra electron, as well as systematic effects more unique to electric field quenching.

### I. INTRODUCTION

In a previous Letter<sup>1</sup> we described a determination of the Lamb shift in hydrogenlike argon based on an electric-field-quenching experiment. Here we present a more complete account of that experiment, as well as a measurement with a one percent error of the unperturbed lifetime of the  $2^2S_{1/2}$  state of hydrogenlike argon. The beam-foil time-of-flight technique was used in both experiments.

In hydrogenlike argon, the  $2^2S_{1/2}$  state decays predominantly by two-photon electric-dipole ( $2E1$ ) decay with a rate of  $2.8 \times 10^8 \text{ s}^{-1}$ , whereas the  $2^2P_{1/2}$  state decays  $2 \times 10^5$  times faster by an allowed electric-dipole ( $E1$ ) decay. In the electric-field quenching experiment an external electric field of known strength mixes the  $2^2S_{1/2}$ -state eigenfunction with the nearby  $2^2P_{1/2}$ -state eigenfunctions, and to a much smaller extent, all other  $nP$ -state eigenfunctions. The lifetime of the electric-field-perturbed  $2^2S_{1/2}$  state is therefore shortened (quenched) by an amount which depends upon the  $2^2S_{1/2}$ - $2^2P_{1/2}$  energy splitting (Lamb shift). Thus, a measurement of the lifetime of the  $2^2S_{1/2}$  state in an external electric field can be used to determine the Lamb shift.

In our earlier publication<sup>1</sup> we reported a value for the Lamb shift in hydrogenlike argon of 38.0(0.6) THz. Since then two new developments result in small changes in the experimental value of the Lamb shift. First, Goldman and Drake<sup>2</sup> have used a relativistic theory to recalculate the unperturbed two-photon decay rate of the  $2^2S_{1/2}$  state of the hydrogen isoelectronic sequence. In hydrogenlike argon their decay rate is 0.35% larger than the relativistic

decay rate calculated by Johnson<sup>3</sup> and used in Ref. 1. Goldman and Drake's result has recently been confirmed by Parpia and Johnson.<sup>4</sup> Using the new value of 3.497 ns for the  $2^2S_{1/2}$  lifetime in determining the total (unperturbed plus quenched) decay rate increases our measured Lamb-shift value<sup>1,2</sup> by approximately 0.1 THz. Second, we have found a procedure which more accurately determines the percentage of  $2E1$  decays which originate from the  $2^1S_0$  state of heliumlike argon. Our new value of 3.5(0.3)% versus our previous value of 3.0(1.0)% lowers the Lamb shift by 0.11 THz and decreases the systematic error from 0.48 THz to 0.17 THz. Taking these, and additional small corrections into account, our value for the Lamb shift in hydrogenlike argon is 37.87(0.38) THz.

### II. DECAY OF THE $2^2S_{1/2}$ STATE

#### A. Theory

In hydrogenlike argon the unperturbed  $2^2S_{1/2}$  state (Fig. 1) decays predominantly by the simultaneous emission<sup>2-10</sup> of two electric-dipole photons ( $2E1$ ). The non-relativistic decay rate has been calculated by many authors and is found to be<sup>10</sup>  $8.229 Z^6$ . In hydrogenlike argon a relativistic decay rate of  $2.768 \times 10^8 \text{ s}^{-1}$  has been calculated by Goldman and Drake.<sup>2</sup> This value which is 0.35% [ $20(Z\alpha)^2\%$ ] larger than the result of an earlier relativistic calculation by Johnson,<sup>3</sup> has been confirmed by Parpia and Johnson.<sup>4</sup>

The  $2^2S_{1/2}$  state also decays by a single-photon relativistic magnetic-dipole ( $M1$ ) decay<sup>3-5,7,11</sup> which scales approximately as  $Z^{10}$ . The  $M1$  decay rate<sup>3,4</sup> in hydrogen-

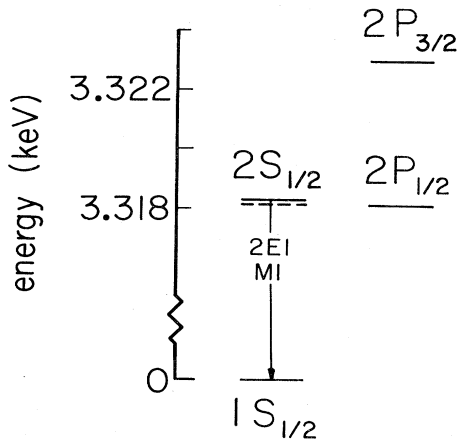


FIG. 1. Energy-level diagram of the  $n=2$  states of hydrogenlike argon. The Lamb shift is 0.16 eV and the  $2^2P_{1/2}-2^2P_{3/2}$  splitting is 4.82 eV. The  $2^2S_{1/2}$  state decays by  $2E1$  and by relativistic  $M1$  decay (3.2%) with a lifetime of 3.5 ns. The relativistic corrections decrease the  $2E1$  decay rate by one percent. The  $2P$  states decay to the ground state by allowed  $E1$  decay with lifetimes of  $1.5 \times 10^{-14}$  s.

like argon is  $9.08 \times 10^6 \text{ s}^{-1}$ . The sum of the  $2E1$  and  $M1$  decay rates give a lifetime of 3.497 ns for the  $2^2S_{1/2}$  state of hydrogenlike argon. Other decay modes to the ground state such as  $2M1$ , two-photon electric-quadrupole, and parity-violating decays are expected to be negligible.<sup>2-4</sup> The allowed  $E1$  decay  $2^2S_{1/2} \rightarrow 2^2P_{1/2}$  is about  $100 \text{ s}^{-1}$ . The radiative corrections to the  $M1$  decay rate vanish in lowest order<sup>12</sup> and radiative corrections to the spontaneous  $2E1$  decay rate are estimated<sup>3</sup> to be of order  $\alpha/\pi \approx 0.1\%$ .

In the unperturbed decay of the  $2^2S_{1/2}$  state the radiation should be isotropic in the rest frame of the decaying atom. There is, however, an angular correlation<sup>5</sup> between the two photons emitted in the decay. The probability of observing two photons whose propagation vectors are at an angle  $\theta$  is proportional to  $1 + \cos^2\theta$ . Au (Ref. 13) has shown that interference between the  $2E1$  and higher multipole terms in the decay can lead to an asymmetry in the angular correlation between the two photons. The magnitude of this effect is predicted to be about  $0.1(Z\alpha)^2$ .

In the  $2E1$  decay of the  $2^2S_{1/2}$  state the theoretical energy distribution<sup>2-5,8-10</sup> of the photons, shown in Fig. 2, is a broad continuum centered at half the  $1^2S_{1/2}-2^2S_{1/2}$  transition energy. The continuum falls rapidly to zero at the end points. The observed spectrum will also show a sharp peak arising from the single-photon  $M1$  decay at the  $2^2S_{1/2}-1^2S_{1/2}$  transition energy<sup>14</sup> of 3318 eV.

## B. Experimental studies of the $2^2S_{1/2}$ state lifetime

### 1. Beam-foil time-of-flight technique

Measurement of the lifetime of both the unperturbed and quenched  $2^2S_{1/2}$  state was performed by the beam-foil time-of-flight method. In our experiment a fast beam

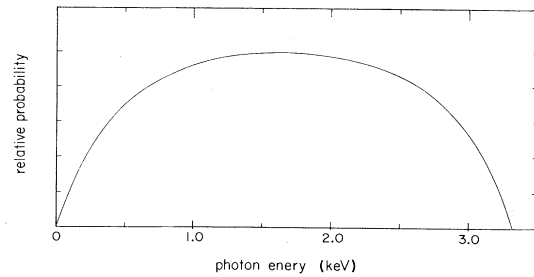


FIG. 2. Theoretical continuum spectra (Refs. 2-5) of the  $2E1$  decay of the  $2^2S_{1/2}$  state of hydrogenlike argon. The relativistic correction decreases the relative intensity near the end points.

of fully stripped  $\text{Ar}^{18+}$  passes through a thin carbon foil where the bare nuclei undergo charge capture. A fraction of the beam emerges as hydrogenlike  $\text{Ar}^{17+}$  in the  $2^2S_{1/2}$  state. The x rays from decays in flight of the  $2^2S_{1/2}$  state as a function of distance downstream from the foil is the raw data in the experiment. The x-ray spectra normalized to the beam intensity is then used to construct decay curves. The decay length and the beam velocity yield the lifetime.

### 2. Beam preparation

The argon ions are obtained from the Lawrence Berkeley Laboratory's Super-HILAC. The ions emerge from the accelerator as  $\text{Ar}^{13+}$  at a velocity of  $4 \times 10^9 \text{ cm/s}$ . At this velocity collisions in a gas or solid target will on average remove electrons from the ions. A sufficiently thick target will produce a charge-state distribution which is independent of both the target thickness and the incident charge state. A charge-state distribution of 61%  $\text{Ar}^{18+}$  (bare nuclei), 33%  $\text{Ar}^{17+}$  (hydrogenlike argon), 5%  $\text{Ar}^{16+}$  (heliumlike argon), and less than 1%  $\text{Ar}^{15+}$  (lithiumlike argon) is observed when the beam passes through a (near equilibrium thickness)  $400\text{-}\mu\text{g/cm}^2$  carbon foil. In addition, the ions lose about 0.5% of their kinetic energy due to collisions in the foil.

By allowing a beam of bare  $\text{Ar}^{18+}$  ions to undergo charge capture in a thin target (where few of the ions can undergo more than one charge-changing collision), a beam containing a very high ratio of hydrogenlike  $\text{Ar}^{17+}$  to heliumlike  $\text{Ar}^{16+}$  is produced. Reducing the fraction of heliumlike argon is crucial to an accurate measurement of the  $2^2S_{1/2}$  lifetime. The lifetime of the  $1^2S_0$  state of heliumlike argon is 2.3 ns.<sup>15-18</sup> It decays by  $2E1$  with an energy spectrum so similar to that of the  $2E1$  decay of the hydrogenlike  $2^2S_{1/2}$  state that the two are indistinguishable in our experiment. (A detailed discussion of this problem is given in section II B 1.)

A schematic diagram of the experimental arrangement is shown in Fig. 3. An analyzing magnet downstream of an equilibrium thickness foil selects the beam of  $\text{Ar}^{18+}$  which then passes through a series of bending and focusing magnets into the experimental area. After collimation, the bare  $\text{Ar}^{18+}$  ions pass through an  $8\text{-}\mu\text{g/cm}^2$  carbon foil. As the foil is much thinner than necessary for charge equilibrium, single-electron capture yielding hydrogenlike

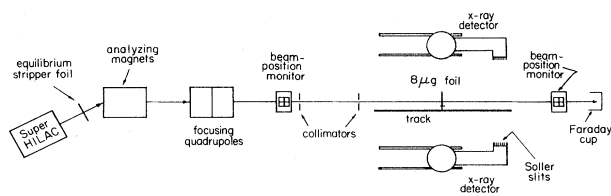


FIG. 3. Schematic diagram of the apparatus used to measure the lifetime of the  $2^2S_{1/2}$  state of hydrogenlike argon. The two x-ray detectors are mounted on tracks and look toward the center of the apparatus. Two-dimensional beam position monitors—phosphor screens which are excited by the beam and viewed remotely by TV cameras—are used to establish the proper beam optics. After a parallel beam is tuned, collimating slits are inserted to reduce the beam size to 0.5 cm wide by 1 cm high and to define the beam axis.

$\text{Ar}^{17+}$  dominates over multiple capture. Among the approximately ten percent of the  $\text{Ar}^{18+}$  which capture electrons in the thin foil, the ratio of hydrogenlike to heliumlike ions is observed to be 16:1. When a  $110\text{-}\mu\text{g}/\text{cm}^2$  foil is substituted, the ratio drops to 12:1, and for  $400\ \mu\text{g}/\text{cm}^2$  it is 7:1.

Following capture in the  $8\text{-}\mu\text{g}/\text{cm}^2$  carbon foil the lithiumlike fraction was too small to observe in the Faraday cup used in the magnetic spectrometer. Measurements of charge exchange<sup>19</sup> at this velocity in  $\text{N}_2$  give an upper limit to the lithiumlike fraction of 1 part in 200 of the hydrogenlike fraction.

### 3. Charge exchange in the residual gas

Charge-changing collisions and quenching collisions in the background gas change the number of ions in the  $2^2S_{1/2}$  state of hydrogenlike argon, introducing a systematic error into the lifetime measurement. In the absence of a foil, no ions other than  $\text{Ar}^{18+}$  were observed. The sensitivity of this measurement sets an upper limit of two percent to the effect of charge-changing collisions on the lifetime.

From the measured charge-changing cross sections<sup>19</sup> for Ar ions in  $\text{N}_2$ , we obtain a much better limit to the change in the number of hydrogenlike argon ions in the  $2^2S_{1/2}$  state due to charge exchange. At  $4 \times 10^9$  cm/s, the cross section for  $\text{Ar}^{18+} \rightarrow \text{Ar}^{17+}$  in  $\text{N}_2$  is  $(0.8 \pm 0.3) \times 10^{-18}$  cm<sup>2</sup>/molecule. (Nitrogen is the principle heavy residual gas in our apparatus. Oxygen has almost the same cross section and lighter elements have smaller cross sections. The cross section for hydrogen is insignificant by comparison.) In the less than  $5 \times 10^{-6}$ -torr pressure inside our apparatus, the probability of  $\text{Ar}^{18+} \rightarrow \text{Ar}^{17+}$  is then less than  $1 \times 10^{-5}$  over a 50-cm flight path. If we assume that a hydrogenlike argon ion produced by collisions in the residual gas has the same probability of being formed in the  $2^2S_{1/2}$  state as a hydrogenlike argon ion produced by collisions in the foil, then with a 10:1 initial ratio of  $\text{Ar}^{18+}$  to  $\text{Ar}^{17+}$ , the ratio of formation in the residual gas to formation in the foil of  $2^2S_{1/2}$  state of hydrogenlike argon is less than  $10^{-4}$ . By the same argument we also find that the contribution to

the  $2^2S_{1/2}$  population from electron loss by heliumlike argon is less than  $10^{-6}$ .

An upper limit to the probability for capture or loss of an electron by a hydrogenlike argon atom in the  $2^2S_{1/2}$  state is obtained by considering lithiumlike  $\text{Ar}^{15+}$ , which consists of a  $2s$  electron outside of a  $1s^2$  core. The lithiumlike  $\text{Ar}^{15+}$  loss cross section in  $\text{N}_2$  is  $(1.8 \pm 0.4) \times 10^{-18}$  cm<sup>2</sup>/molecule. The  $\text{Ar}^{15+}$  capture cross section on the other hand is smaller than the  $\text{Ar}^{17+}$  loss cross section, so the hydrogenlike argon ground-state cross section is an upper limit. From these cross sections, we find that under our experimental conditions, the probability for destroying the hydrogenlike argon  $2^2S_{1/2}$  state by charge exchange is less than  $2.2 \times 10^{-5}$  over a 50-cm path. Since the  $2^2S_{1/2}$  decay length is only 14 cm the change in the apparent  $2^2S_{1/2}$  lifetime is nil.

### 4. Collisional quenching

An upper limit to the total charge changing plus collisional quenching cross sections can be obtained by observing the count rate from a (very long lived) state as a function of background pressure. This test was performed<sup>20</sup> on the  $2^3S_1$  state of heliumlike argon which has a lifetime<sup>21</sup> of 208 ns. As the  $2^3S_1$  state is formed from a  $2s$  electron plus an electron in the ground state it is a reasonable approximation to the  $2^2S_{1/2}$  state for collisional quenching studies. The count rate from the decay of the  $2^3S_1$  state, observed 165 cm downstream from the foil, changed by less than one-half percent when the background pressure in the apparatus was raised from  $3 \times 10^{-6}$  torr to more than  $10^{-5}$  torr. This sets an upper limit to the collisional quenching cross section (at  $4 \times 10^9$  cm/s) of  $10^{-16}$  cm<sup>2</sup>/molecule. The collisional quenching of the  $2^2S_{1/2}$  state then decreases the apparent  $2^2S_{1/2}$  decay length by less than 0.11%.

A collisional quenching cross section of less than  $10^{-16}$  cm<sup>2</sup>/molecule is consistent with experiments of Matthews and Fortner,<sup>22</sup> who find a collisional quenching cross section of  $0.7(0.2) \times 10^{-16}$  cm<sup>2</sup>/atom for the  $2^3P_1$  state of heliumlike fluorine at a velocity of  $1.7 \times 10^9$  cm/s in neon.

### 5. Detection of x rays

The x rays from decays in flight of excited states are observed by a pair of lithium-drifted silicon, guard-ring x-ray detectors<sup>23</sup> (Fig. 3). The x-ray detectors are located approximately 60 cm from the beam and collimated by Soller slits<sup>24</sup> to view a 2-cm-long portion of the beam. The x-ray detectors have a range of motion, parallel to the (undeflected) beam axis, of 30 cm. In addition the  $8\text{-}\mu\text{g}/\text{cm}^2$  carbon foil is mounted on a shaft and can be translated about 100 cm. The combined motion of the foil and detectors allows observations of the decays over a length of 70 cm. The positioning accuracy of the foil is 0.5 mm and of the detectors 0.05 mm and the distance between the x-ray detectors and the beam axis varies by less than 0.25 mm over the 30-cm travel.

The instrumental line shape of the x-ray detectors can be modeled to a Gaussian plus a low-energy and a small

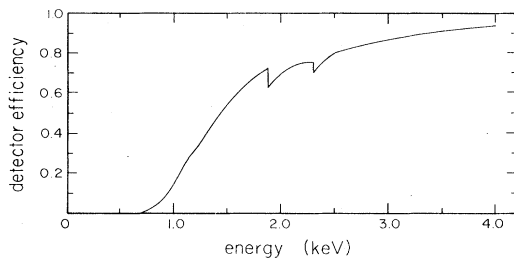


FIG. 4. X-ray detector efficiency as a function of the incident photon energy. Above 10 keV the efficiency begins to drop as the photons pass through the active portion of the detector without being absorbed.

high-energy exponential tail. The exact instrumental line shape for a source moving at  $4 \times 10^9$  cm/s was determined from observations of the 3.1-keV x ray from the 208 ns lifetime  $M1$  decay<sup>21</sup> of the  $2^3S_1$  state of heliumlike argon. We observed a full-width at half-maximum linewidth of 280 eV at 3.1 keV.

The x-ray detector efficiency is close to 100%. However, there is photoelectric absorption and a small amount of inelastic and Compton scattering in a silicon dead layer, a gold conductive coating and especially in a beryllium window. The absorption cross sections<sup>25</sup> for Be and Si are highly energy dependent below 2.0 keV. A plot of the x-ray detector efficiency as a function of photon energy is shown in Fig. 4. Measurements used to determine the x-ray detector efficiency and additional details of their spectral response are discussed in section III C 5.

#### 6. X-ray spectra from decays in flight

To compare the observed spectra with the theoretical spectra, we convoluted the Gaussian response function of the detector with the product of the theoretical  $2^2S_{1/2}$  two-photon spectrum in Fig. 2 and the x-ray detector efficiency in Fig. 4. Small peaks, at the  $2P-1S$  single-photon transition energies of hydrogenlike and heliumlike argon, were also added. The result shown in Fig. 5 is a good approximation to the observed spectra which are shown in Figs. 6(a)–6(g), particularly Figs. 6(a) and 6(b), where the ratio of counts in the peak and in the two-photon spectra are similar to Fig. 5.

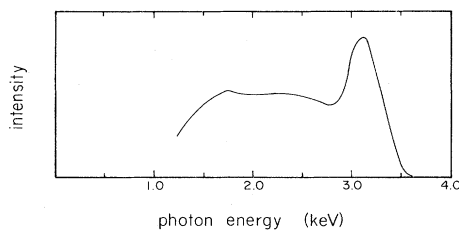


FIG. 5. Calculated x-ray detector response to the decay spectrum of hydrogenlike argon plus a small fraction of heliumlike argon. The x-ray detector efficiency (Fig. 4) and instrumental line shape are convoluted with the  $2E1$  spectra (Fig. 2) plus single-photon peaks at 3.1 keV and 3.3 keV.

Figures 6(a)–6(g) show the x-ray spectra from the decays in flight as a function of the distance downstream from the foil. In addition to the two-photon continuum there is a peak near 3.2 keV. A least-squares fit using the x-ray detector line shape<sup>26</sup> shows that the peak has two components separated by 205(20) eV. The largest contribu-

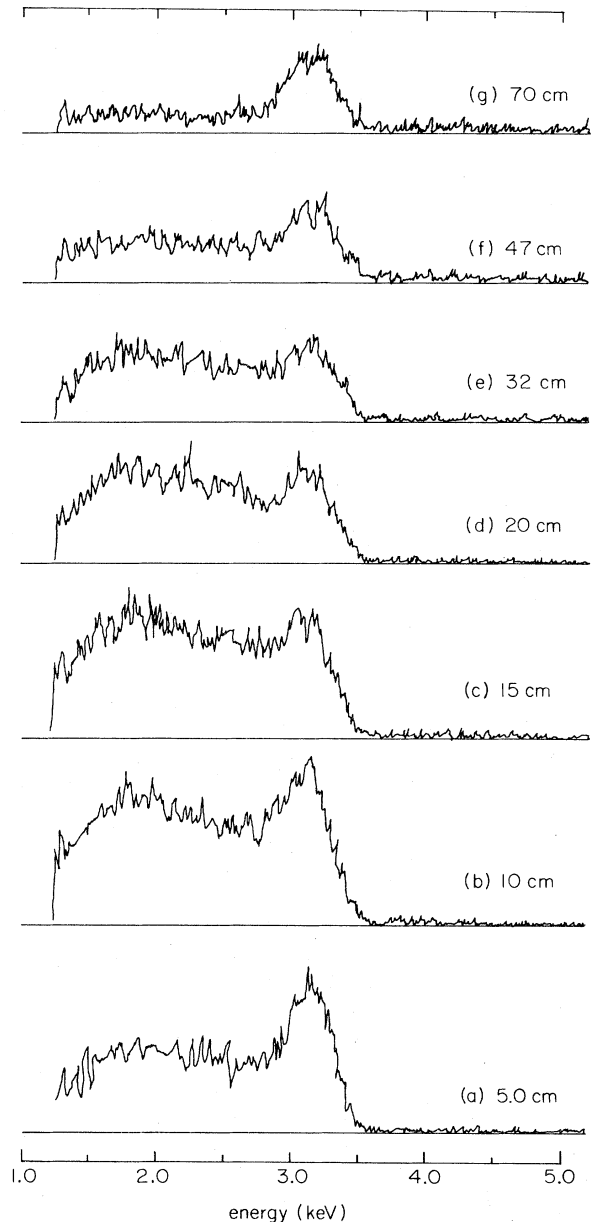


FIG. 6. (a)–(g) Observed spectra from decays in flight of hydrogenlike argon (and a small amount of heliumlike argon) as a function of distance downstream from the thin foil. Two peaks, not quite resolved, can be seen in the spectra at large distances downstream from the foil where the  $2E1$  contribution is small. The ratio of intensities of the peak to two-photon continuum can be seen to first decrease and then increase as a function of distance downstream from the foil suggesting that something besides  $M1$  decay contributes to the peak.

tion to the 20-eV uncertainty is the presence of the two-photon continuum which the fitting program treats as a large energy-dependent background. Within the uncertainty we find the separation of the peaks to be independent of the distance downstream from the foil. The 205-eV peak separation corresponds to the difference in transition energies from the  $n=2$  states of hydrogenlike and heliumlike argon.<sup>27</sup> In particular, the single-photon  $n=2 \rightarrow n=1$  hydrogenlike decays produce photons approximately 199 eV higher than the heliumlike  $2^3P_2 \rightarrow 1^1S_0$  magnetic-quadrupole ( $M2$ ) decay and roughly 217 eV higher than the 208 ns  $2^3S_1 \rightarrow 1^1S_0$  magnetic-dipole decay.

### 7. Decay curves from one-photon decays

Decay curves constructed from fits to the single-photon transitions in heliumlike and hydrogenlike argon are shown in Fig. 7(a) (heliumlike) and Fig. 7(b) (hydrogenlike). The spectra used are those in Figs. 6(a)–6(g) and additional spectra. Also shown in Fig 7(a) is a least-squares fit of a single exponential plus a constant background to the decay curve. The decay length and amplitude of the exponential, and the amplitude of the background were allowed to vary. The resulting lifetime of 1.6(0.2) ns, is consistent with the 1.51-ns calculated,<sup>28</sup> and 1.62(0.08)-ns measured<sup>15,29</sup> lifetime of the  $2^3P_2$  state of heliumlike argon. The  $M1$  decay of the  $2^3S_1$  state with a decay length of 830 cm is not apparent but is an important contribution to the “constant” background.

The decay curve in Fig. 7(b), constructed from the hydrogenlike argon one-photon decay peak, has several components. The contribution from the single-photon  $M1$  decay of the  $2^2S_{1/2}$  state is plotted as the broken line in Fig. 7(b). We calculate the  $M1$  intensity from the ratio of the  $M1$  and  $2E1$  decay rates in Refs. 2–4, and the intensity of the two-photon continuum normalized to the x-ray detector efficiency. The  $M1$  decay does not account for the full amplitude of the decay curve. In addition, a single exponential plus a constant background does not satisfac-

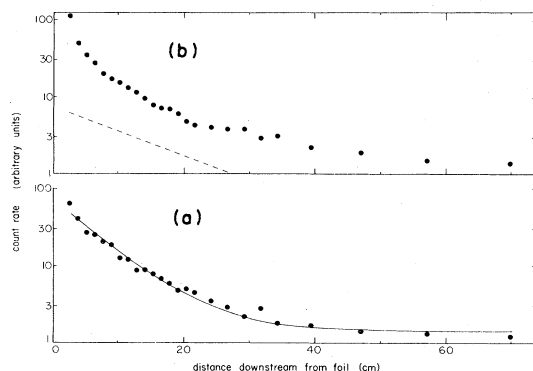


FIG. 7. (a),(b) Decay curves from the single-photon decay of the  $n=2$  states of (a) heliumlike argon and (b) hydrogenlike argon. In (a), the line through the points is a least-squares fit of a single exponential plus a constant background to the decay curve. In (b), the broken line is the (calculated)  $M1$  contribution to the decay curve.

torily fit the decay curve. The logical explanation is that a large fraction of the observed count rate in the single-photon hydrogenlike argon spectra arises from cascade-fed decays of the  $2^2P_{1/2}$  and  $2^2P_{3/2}$  states.

(Position-dependent background can be ruled out as an explanation of our observations. The two-photon continuum shows no observable background for nearly five decay lengths, and the count rate in the absence of a foil is virtually nil.)

### 8. Cascade feeding of the $2P$ states

Decays of cascade-fed  $2P$  and some higher  $P$  states have been measured in hydrogenlike oxygen,<sup>30,31</sup> hydrogenlike nitrogen,<sup>31</sup> hydrogenlike carbon, hydrogenlike boron, and in heliumlike fluorine<sup>32</sup> and heliumlike oxygen.<sup>31</sup> As with the decay curve in Fig. 7(b), the data in Refs. 30–32 could not be satisfactorily fitted by a single exponential. They were, however, well fitted by a power curve of the form  $y=At^{-n}$  where  $n$  was found to be between 1.5 and 1.6.

A number of authors<sup>33</sup> have developed models for cascade feeding of the  $2P$  states which predict the observed power dependence. To compare these models and the experiments in Refs. 30–32 with our observations, we subtracted the estimated  $M1$  contribution from the data in Fig. 7(b) and fitted the resulting decay curve to the form  $y=At^{-n}$ . The best fit to the data is shown in Fig. 8, where we find  $n=1.53(0.10)$ , in agreement with the models<sup>33</sup> and other experiments.<sup>30–32</sup>

Although cascade feeding of the  $2P$  states is expected to be as strong in heliumlike argon as in hydrogenlike argon, at distances of a few cm downstream from the foil there is little evidence of cascade feeding in heliumlike argon. This is due to the presence of the strong lines from the single-photon decays of the metastable  $2^3P_2$  and  $2^3S_1$  states. From the  $2^2P_{1/2}$  cascade rate in hydrogenlike argon and the ratio of  $\text{Ar}^{17+}$  to  $\text{Ar}^{16+}$  we estimate that cas-

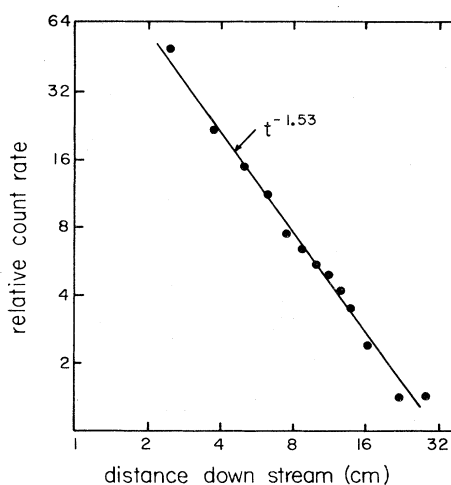


FIG. 8. A log-log plot of the data in Fig. 7(b) after subtracting the  $M1$  component. The line through the points is the least-squares fit to the data of a power curve  $y=At^{-n}$ . A value of  $n=1.5$  is strongly associated with cascade-fed decays of the  $2P$  states.

cadesc into the short-lived  $2^3P_1$  and  $2^1P_1$  states account for approximately 10% of the count rate in the decay curve in Fig. 7(a).

### 9. Cascade feeding of the $2^2S_{1/2}$ state

In hydrogenlike argon there are presently no experiments which resolve the single-photon  $M1$  decay of the  $2^2S_{1/2}$  state from the  $E1$  decay of the  $2^2P_{1/2}$  state. Cascade feeding of the  $2P$  states is therefore a serious obstacle to the study of the one-photon decay of the  $2^2S_{1/2}$  state; both for measurements of the natural lifetime and for electric-field-quenching experiments.

The  $2E1$  decay of the  $2^2S_{1/2}$  state, however, can be studied free from interference from the cascade-fed decays of the  $2P$  states. The remaining problem is then to what extent cascades feed the  $2^2S_{1/2}$  state. Any cascades which populate the  $2^2S_{1/2}$  state in the measurement region will cause the measured  $2^2S_{1/2}$  lifetime to be longer than the true lifetime. From both experimental studies of hydrogenlike argon and from theory we will show that 1 ns after passing through the foil (4 cm), the cascade rate to the  $2^2S_{1/2}$  state is negligible.

The transition probabilities for  $E1$  decay of states of moderately high principal quantum number  $n$  and orbital angular momentum  $l$ , exhibit a large branching ratio for transitions in which  $n$  decreases by more than one. As the angular momentum can only change by one unit in  $E1$  decay, there is a high probability that in a sequence of de-

cays, a state of maximum angular momentum,  $l = n - 1$ , will be reached (yrast state). From any yrast state virtually all cascades reach the  $2P$  states.

Examples of decays from high  $n, l$  states are shown in Figs. 9(a)–9(d). In Fig. 9(a) we show the results of our calculation<sup>34</sup> of the branching ratios for the decay paths from the  $n = 18, l = 12$  state of hydrogenlike argon. From this state the probability that a sequence of decays will cascade to the  $2^2S_{1/2}$  state is only  $5 \times 10^{-4}$ . The most probable decay path from the  $n = 18, l = 12$  state to the  $2^2S_{1/2}$  state has a cumulative decay time of 1.8 ns. In Figs. 9(b)–9(d) we see that as  $l$  decreases the fraction of cascades to the  $2^2S_{1/2}$  state increases. However, the lower- $l$  states and the states to which they decay have lifetimes which are much shorter than either the yrast states or the high- $l$  states. The cascade times from the low- $l$  states to the  $2^2S_{1/2}$  state are therefore much shorter than the  $> 1$  ns between excitation in the foil and the first data point on our decay curve. The worst case is that of a high- $nS$  state shown in Fig. 9(d). Some 12% of these decay to the  $2^2S_{1/2}$  state and because the transition rate is much smaller for  $n$  and  $l$  to change in the opposite sense, the high- $nS$  states have longer lifetimes than other low- $l$  states. Even here, however, the lifetimes are still quite short; the cascade time from the  $18^2S_{1/2}$  state to the  $2^2S_{1/2}$  is less than 0.12 ns.

We can obtain a simple estimate of the cascade rate to the  $2^2S_{1/2}$  state by applying an "average" branching ratio for cascades from high- $n, l$  states to the observed cascade

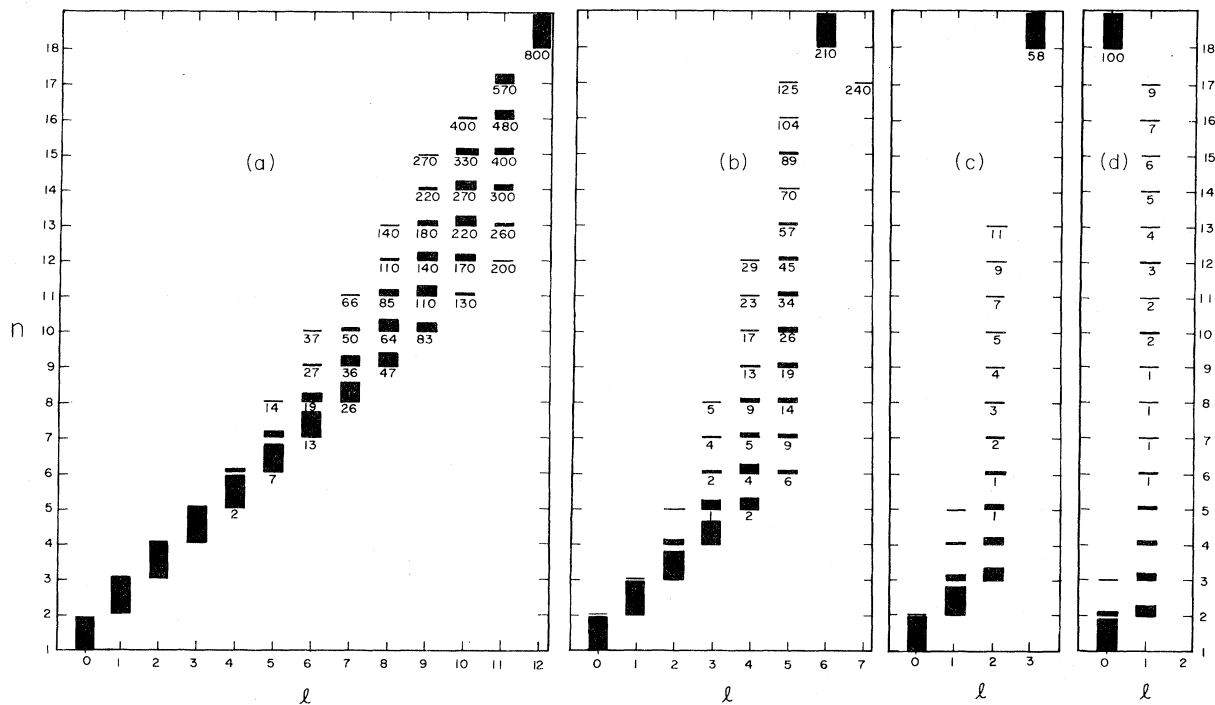


FIG. 9. (a)–(d) Cumulative branching ratios calculated for  $E1$  decay of the  $n = 18$ ; (a)  $l = 12$ , (b)  $l = 6$ , (c)  $l = 3$ , and (d)  $l = 0$  states of hydrogenlike argon. The height of the bars above each state indicates the fraction of the initial  $n = 18$  population which decays to that state (full height = 100%). The numbers beneath the states are their lifetimes in ps. In (a)–(c) each successive decay changes  $l$  by  $-1$  and the populations move right to left. In (d) the cascade is  $18^2S_{1/2} \rightarrow nP \rightarrow nS$ .

rate to the  $2^2P$  states shown in Fig. 8. This procedure gives a cascade rate which after a few ns drops to less than  $5 \times 10^{-4}$  of the natural decay rate of the hydrogenlike argon  $2^2S_{1/2}$  state.

#### 10. Experimental determination of cascade feeding of the $2^2S_{1/2}$ state

A completely rigorous upper limit to the cascade rate to the  $2^2S_{1/2}$  state can be determined from the experimental data. Any cascade to the  $2^2S_{1/2}$  state must make a transition from a  $n^2P$  state with  $n > 2$ . However, decay from the  $n^2P$  to the  $1^2S_{1/2}$  state (Lyman series) is 7 to 8 times more probable than decay to the  $2^2S_{1/2}$  state. Thus for every seven decays observed in the Lyman series, there is on average only one decay to the  $2^2S_{1/2}$  state. The spectra of the Lyman series transitions in hydrogenlike argon lie between 3.9 and 4.4 keV. If present, they are readily observable in our spectra.

In the spectra shown in Figs. 6(a)–6(g), there are counts which by their energy and separation from the  $n=2 \rightarrow n=1$  spectra we identify as possible members of the Lyman series. The spectra extends from the  $3^2P-1^2S_{1/2}$  transition at 3.9 keV to the series limit at 4.4 keV. There is also background present in the spectra. In many of the spectra the background is larger than the counts from the Lyman series transitions, but they are difficult to distinguish and to obtain an upper limit it does no harm to include the background.

As an example of the calculation, consider the spectra shown in Fig. 6(a). Observed 5 cm downstream from the foil (1.25 ns after excitation), there are some 50 counts in the 3.9–4.4 keV region. In the two-photon continuum, between 2.0 keV and 2.5 keV there are 2100 counts from  $2E1$  decay. To compare these numbers we apply two corrections: First, the probability that a photon emitted in a  $2E1$  decay has an energy<sup>2-5,8-10</sup> between 2.0 keV and 2.5 keV is 0.36. Second, we correct for the approximately 20% higher x-ray detector efficiency at the higher x-ray energy. Then, using a value of 7.5 to 1 for the ratio of decay of  $n^2P \rightarrow 1^2S_{1/2}$  to the decay of  $n^2P \rightarrow 2^2S_{1/2}$ , we find an upper limit of  $1 \times 10^{-3}$  cascades per  $2^2S_{1/2}$  state decay at 5 cm downstream from the foil.

Examining spectra taken at larger distances downstream from the foil, we find the ratio of cascades to decays gradually increases. The ratio is  $0.9 \times 10^{-3}$  at 0.3 mean lives (1 ns),  $1.8 \times 10^{-3}$  at 2.3 mean lives (8 ns), and is nearly constant at  $4 \times 10^{-3}$  beyond 2.3 mean lives.

To calculate the change in the observed lifetime from the varying cascade rate to the  $2^2S_{1/2}$  state we constructed a model of a single exponential decay curve with a lifetime of 3.5 ns. Counts corresponding to the cascade rate at different distances were added to the decay curve, and a single exponential was least-squares fitted to the resulting curve. The increase in the lifetime was 0.17%. Background in the 3.9–4.4-keV region accounts for some of the counts at small distances downstream from the foil and probably accounts for most of the counts at large distances. We consequently assign an error to this value of  $-0.12\%$ ,  $+0\%$ .

Finally, we consider if a decay of an excited state can

produce a photon with the same energy as a photon from the  $2E1$  decay of the  $2^2S_{1/2}$  state. The answer is no. In hydrogenlike argon the gap in the spectrum of  $E1$  radiation between the Balmer series limit of 1100 eV and the Lyman  $\alpha$  at 3318 eV assures an absence of interfering hydrogenlike argon lines in this region. The decay curves for the  $2^2S_{1/2}$  state lifetime in hydrogenlike argon are constructed from the portion of the two-photon continuum between 2.0 keV and 2.5 keV.

#### 11. Interference from the $2E1$ decay of heliumlike argon

In the helium isoelectronic sequence all single-photon transitions from the  $2^1S_0$  to the  $1^1S_0$  ground state are rigorously forbidden. The  $2E1$  decay is necessarily the only important decay mode of this state. The  $2E1$  rate has been calculated in heliumlike ions by several authors.<sup>15-18</sup> For heliumlike argon, the calculated lifetimes of 2.35 ns<sup>15</sup> and 2.48 ns<sup>18</sup> are in agreement with the value of 2.3(0.3) ns measured by Marrus and Schmieder.<sup>15,35</sup>

The  $2E1$  decay of the  $2^1S_0$  state of heliumlike argon (Fig. 10) produces a continuous spectrum extending to 3.2 keV with an energy distribution<sup>5,17,18</sup> nearly identical to that from the  $2E1$  decay of hydrogenlike argon.<sup>2-5,8-10,15</sup> No experimentally practical way of separating the spectra has been found. As the heliumlike  $2^1S_0$  state has a shorter lifetime than the hydrogenlike  $2^2S_{1/2}$  state its presence in the beam will cause the  $2^2S_{1/2}$  lifetime obtained from the two-photon spectra to be shorter than the true  $2^2S_{1/2}$  lifetime. Model calculations show, for example, that if 1% of the  $2E1$  counts arise from the  $2^1S_0$  decay, the measured lifetime will appear 0.4% shorter than the true  $2^2S_{1/2}$  lifetime.

In heliumlike atoms the  $n=2$  population is distributed over a larger number of substates than in hydrogenlike atoms. Consequently, we expect that the population ratios of  $2^2S_{1/2}$  to  $2^1S_0$  will be larger than the 16:1 ratio of  $\text{Ar}^{17+}$  to  $\text{Ar}^{16+}$  which we observe in the  $\text{Ar}^{17+}$  enriched beam.

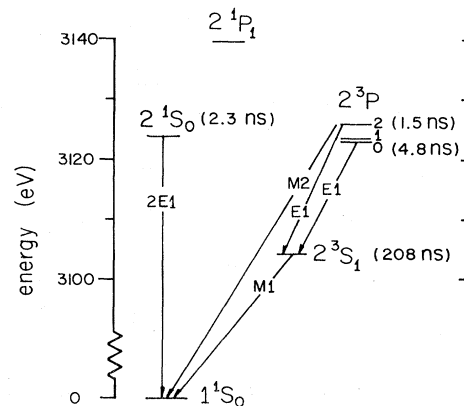


FIG. 10. Energy levels of the  $n=2$  states of heliumlike argon (Ref. 27) and decay modes and lifetimes of long-lived states.

## 12. Measurements of the $2^1S_0:2^2S_{1/2}$ ratio

*a. Previous measurement.* In Ref. 1 we described how a series of comparisons were used to estimate the fraction of decays which originate from the  $2^1S_0$  state. We compared the intensity of the  $2^2S_{1/2}$  radiation with the intensity of the peak from the magnetic-quadrupole ( $M2$ ) decay of the  $2^3P_2$  state of the heliumlike contaminant. This established a  $2^2S_{1/2}$  to  $2^3P_2$  population ratio. A population ratio of heliumlike  $2^3P_2$  to  $2^1S_0$  was obtained by comparing the intensity of the  $M2$  decay  $2^3P_2 \rightarrow 1^1S_0$  with the intensity of the  $2E1$  spectra in a beam which was enriched in heliumlike argon.<sup>15,36</sup> By combining the two ratios we found that the  $2^1S_0$  population was 3.0(1.0)% of the initial  $2^2S_{1/2}$  state population. We ascribed a large error to this measurement because of the possibility of interference from cascades in the single-photon decays, contamination of the enriched heliumlike beam with hydrogenlike argon, and the accumulation of errors from the separate measurements.

*b. A new determination.* The uncertainty in the measured  $2^1S_0$  fraction was the largest source of error in our Lamb-shift experiment and we considered it important to obtain a more direct and accurate measurement of the  $2^1S_0$  to  $2^2S_{1/2}$  ratio. After some ambitious failures, we devised a simple procedure, which gives reproducible results and is free from most of the problems of the ratio measurement in Ref. 1. Our procedure is based upon the fact that the contaminant is small. We use the approximate measured  $2^2S_{1/2}$  and  $2^1S_0$  lifetimes to fit two exponentials to a decay curve from a beam containing a known ratio of hydrogenlike  $Ar^{17+}$  to heliumlike  $Ar^{16+}$ . The  $t=0$  intercepts of the two exponentials give the ratio of  $2^1S_0$  to  $2^2S_{1/2}$  relative to the charge-state fractions in the beam and the respective decay rates. For this technique to be effective the beam must contain a larger ratio of heliumlike  $Ar^{16+}$  to hydrogenlike  $Ar^{17+}$  than present in the beam used in our lifetime measurements. A meaningful result cannot be obtained from our hydrogenlike argon-enriched beams because in the hydrogenlike argon enriched beams the contribution from the  $2^1S_0$  state is as small as the scatter in the data. Early studies<sup>36</sup> of the  $2^2S_{1/2}$  state of hydrogenlike argon used beams which did not have the high hydrogenlike argon to heliumlike argon ratio used in the later experiments.<sup>15,37</sup> These argon beams formed by passing  $Ar^{13+}$  through a  $50\text{-}\mu\text{g}/\text{cm}^2$  foil had ratios of hydrogenlike argon to heliumlike argon of 2.1 to 1.0. In addition, the beams used in Refs. 15, 35, and 36 to measure the heliumlike  $2^1S_0$  lifetime were heliumlike argon enriched, having a ratio of hydrogenlike argon to heliumlike argon of 1.0 to 6.75.

Four decay curves, two for each of the charge-state ratios ( $Ar^{17+}$  to  $Ar^{16+}$  of 2.1 to 1 and 1 to 6.75) were fitted to the sum of two exponentials plus a constant background. A lifetime of 3.5 ns was used for one component. For the second component, 2.35 ns was used for the data with the larger fraction of hydrogenlike ions. In fitting the two decay curves from the heliumlike argon enriched beam the  $2^1S_0$  lifetime was allowed to vary. From fits to the four decay curves, we find that at  $t=0$  hydrogenlike argon is in the  $2^2S_{1/2}$  state an average of 1.78(0.20) times

as often as a heliumlike argon is in the  $2^1S_0$  state. In the hydrogenlike argon enriched beams used in our lifetime measurements (a 16:1.0 ratio of  $Ar^{17+}$  to  $Ar^{16+}$ ) the  $2^1S_0$  fraction is 0.035(0.004) of the  $2^2S_{1/2}$  state. This agrees with the less precise value of 0.030(0.01) in Ref. 1.

The fit to the decay curve from the heliumlike enriched beams gives a  $2^1S_0$  lifetime of 2.32(0.2) ns; a slight improvement over the earlier value<sup>15,35</sup> of 2.3(0.3) ns obtained from the same data and in agreement with theory.<sup>15,18</sup>

## 13. Measurement of beam velocity

To determine the mean life of the state from the beam-foil-time-of-flight method, the beam velocity must be accurately known. In the case of the Super-HILAC, the beam velocity is not precisely determined by the operating conditions of the accelerator.

The Super-HILAC<sup>38</sup> is a linear accelerator in which ions are accelerated by an alternating rf field. To prevent a reverse acceleration when the electric field reverses, the ions are shielded by drift tubes placed at increasing intervals along the linac. Within limits set by the drift tube spacing, the beam velocity may depend upon the rf field strength and phase between the different sections of the linac. An uncertainty in the beam velocity of a few percent and a velocity spread of about 0.5% are typical for any particular set of operating conditions. The low selectivity will occasionally allow a lower charge state of the same atom to be accelerated to a lower final energy, often with similar magnetic rigidity. For this reason magnetic rigidity measurements of the beam velocity cannot be relied upon unless the charge state is simultaneously measured.

Our approach was to use silicon surface-barrier detectors, which measure the total kinetic energy of the ion independent of its charge.<sup>23</sup> When heavy ions are stopped in a surface-barrier detector a small part of the energy loss does not contribute to the production of electron-hole pairs.<sup>23,39</sup> For ions of mass 40 in a detector which has not been radiation damaged, the largest contribution to this pulse-height defect occurs at the end of the ions' range. The pulse-height defect for argon ions rises slowly at energies above a few MeV/nucleon and is about 1% at 8.5 MeV/nucleon (340 MeV). To accurately measure the energy of the argon ions only a single calibration point near 340 MeV is necessary.

To calibrate our surface-barrier detectors (Fig. 11) we used a beam consisting of about 1 particle /s of  $^{40}Ar^{10+}$  at 346.47 MeV. The beam was obtained from the Lawrence Berkeley Laboratory's 88 inch sector-focused cyclotron and analyzed in-line by a magnetic spectrometer<sup>40</sup> consisting of a pair of  $110^\circ$  flat field, edge-focusing bending magnets. The energy resolution of this system is 0.02% with a long-term stability of two parts in  $10^5$ . The system had previously been calibrated<sup>40</sup> against the proton resonance in  $^{12}C$  at 14.233 MeV.

The charge collected from the surface-barrier detector is matched in a preamplifier by injecting the output of a precision-tailed pulser across a low-temperature-coefficient capacitor. The pulser contains a variable dc

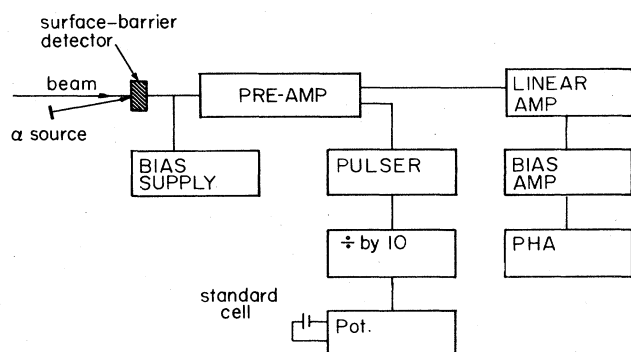


FIG. 11. Schematic diagram of the beam-energy measuring system. Precision pulsers are calibrated against a beam of 346.47-MeV argon ions from the 88-in. cyclotron and an  $\alpha$  source. The  $\alpha$  source is later used to test for radiation damage to the surface-barrier detectors and long-term drift in the electronics. Two pulsers, four surface barrier detectors, and two preamplifiers were used to provide redundancy.

voltage source which is chopped by a relay. The dc voltage of about 8 V is measured against a standard cell using a Leeds and Northrop model K4 potentiometer and a precision divider. Before and after our experiment, the standard cell was checked against a bank of stabilized standard cells. The surface-barrier detectors (ORTEC model A-023-025-300T) have an active area of 25 mm<sup>2</sup> and a depletion depth of 300  $\mu$ m. The range<sup>41</sup> of 340-MeV argon in Si is about 115  $\mu$ m. A large charge-collection capacitor was used in the preamplifiers to keep the preamplifier gain insensitive to the small differences in capacitance between different surface-barrier detectors. We used the same cables between the pulser and the preamplifier for both the calibration and the experiment and kept the distance between the detector and the preamplifier short.

In addition to the 346.47-MeV argon ions, the detectors were at the same time calibrated against the 8.785 MeV, 6.09 MeV, and 6.05 MeV  $\alpha$ 's (Ref. 42) from the <sup>212</sup>Po and <sup>212</sup>Bi daughters of <sup>212</sup>Pb. After one year, the pulser calibration measured against the  $\alpha$  energies had changed by only 0.2%.

Each of four surface-barrier detectors were calibrated against the 346.47-MeV argon ions and the  $\alpha$ 's with two different pulsers. The entire procedure was then repeated using a second preamplifier. We estimate the error in the argon energy calibration to be 0.2%; mostly due to uncertainty in locating the centers of the pulse-height distributions. Our error in measuring the energy of the argon ions at the Super-HILAC is about 0.4% (0.2% in the velocity). The main contributions are the spread and drift of the beam velocity, temperature variations,<sup>43</sup> and calibration error.

#### 14. Normalization of the count rate

The count rate from each x-ray detector was normalized to the total current obtained by stopping the beam in a Faraday cup. The Faraday cup output was measured by a Brookhaven Instruments Corp. model 1000C integrating

electrometer. A correction for the dead time in each detector incorporated into the normalization is described below.

Following the arrival of an x ray or other ionizing radiation (event) the detector and counting system has a dead time during which it is unavailable to detect another event. In our system 55  $\mu$ s is typically required to detect, analyze and store the signal produced by a 3-keV x ray. The Super-HILAC operates in a pulsed mode with a duty factor of about 15%. An average count rate of 25 3-keV x rays per second causes a dead time of one percent.

In addition to these soft x rays, high-energy photons, charged particles, and especially neutrons make major contributions to the dead time. Since the energy of the argon beam at 8.5 MeV/nucleon is above the Coulomb barrier, these neutrons are produced in copious quantities in collisions with the foil, the collimators and the Faraday cup. Energies of several hundred keV and higher are deposited<sup>23</sup> in the detector by 1-MeV to 10-MeV neutrons; energies of tens of MeV are sometimes deposited by scattered ions, and lesser energies by Compton scattered high energy photons. The amplifiers, when presented with signals one hundred or one thousand times their full scale range require from 1 to 100 ms to recover.

Our procedure for automatic dead-time correction is shown in schematic form in Fig. 12 and a timing diagram is shown in Fig. 13. The output from the Faraday cup is amplified and split into two channels. Each channel is fed into a separate integrating electrometer. A gate at the input of each electrometer prevents the electrometer from storing charge during the time that the x-ray detector, the electronics, and the computer access channel associated with that electrometer is unable to detect an event. The time required to turn on and off each gate is 200 ns, shorter than the time period of any observable structure in the Super-HILAC beam pulse.

Each busy signal is derived from busy signals produced by an x-ray detector, its amplifier, analog-to-digital converter (ADC), and computer access channel. A fast discriminator at the x-ray-detector preamplifier output detects the presence of an event in a maximum of 1  $\mu$ s and triggers a busy pulse of about 8- $\mu$ s duration. (The fast discriminator is similarly used to prestart the logic for pile-up rejection.) After about 5  $\mu$ s a slow discriminator

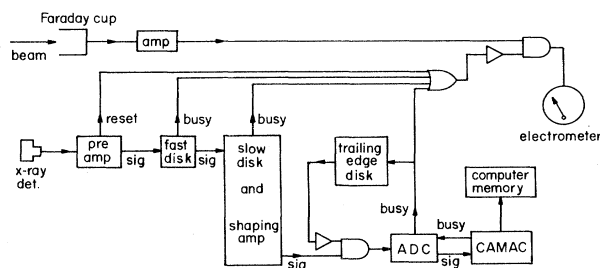


FIG. 12. Schematic diagram of one channel of the automatic dead-time correction system. The system was tested by varying the beam intensity. When the intensity was increased a factor of 12, raising the dead time from 1% to 12%, the normalized count rate changed by only 1.0(1.0)%.

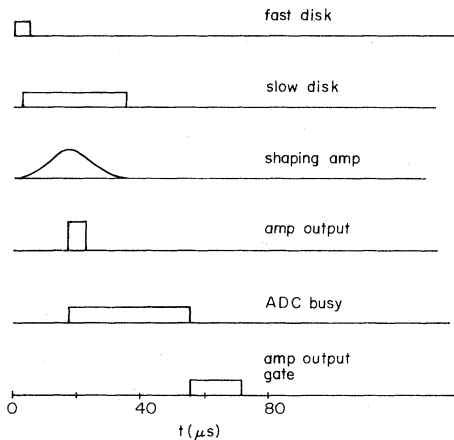


FIG. 13. The sequence of pulses in the x-ray detector electronics and the dead-time correction system following detection of a low-energy x ray.

has detected the event and a detector busy signal is present until the detector is again ready (in about  $35 \mu\text{s}$ ). The outputs of the fast and slow discriminators are sent through an "or" gate with the ADC busy signal, and a reset busy pulse. The reset busy pulse is generated by the x-ray detector preamplifier when the charge-collection capacitor is discharged. This occurs when charge corresponding to several MeV of total energy is accumulated.

The ADC generates a busy signal which does not clear until the ADC receives a signal that its output has been read and the computer access channel is cleared. If the ADC does not clear in  $17 \mu\text{s}$  the x-ray detector will be ready while the logic described above indicates that the system is still busy. To correct this overstatement of the dead time, a pulse of  $17\text{-}\mu\text{s}$  duration (equal to the rise time in the x-ray-detector shaping amplifier) is generated at the end of the ADC busy and is used to block the output of the x-ray detector.

We tested the dead-time correction by measuring the

normalized x-ray count rate from the beam as a function of the system dead time. At count rates which produced 12% dead time we observed a normalized count rate which was 1.0(1.0)% lower than the count rate observed when the dead time was only a few percent. We typically took data with the dead time at from three percent to five percent. The error in the count rates due to the error in dead-time corrections would then be 0.25(0.25)% to 0.4(0.4)%. These values will be smaller if the dead-time error versus dead time is quadratic. In most decay-curve measurements we were able to vary the intensity of the beam so as to keep the dead time uniform over several mean lives. This reduced the variation in the dead time error to a few parts per thousand.

#### 15. Decay curves from the $2^2S_{1/2}$ two-photon spectra

Figure 14 shows the decay curves obtained from the two-photon spectra. The 23 points in each decay curve (two detectors) were obtained by integrating the typically 2500 counts in the portion of the spectra between 2.0 keV and 2.5 keV. Some of the spectra are shown in Figs. 6(a)–6(g). We applied a small correction to the raw data to account for the tail of the one-photon decay peaks which extend below 2.5 keV. The count rate was normalized to the integrated beam current and corrected for system dead time as described in the previous section. At 8.5 MeV/amu the energy deposited in the  $8\text{-}\mu\text{g}/\text{cm}^2$  carbon foil is small and changes in the normalization due to foil aging are not significant over short times. (A single foil survived the entire set of Lamb-shift and lifetime measurements.)

The data were taken at distances from 5 cm to 70 cm downstream from the foil. Between 5 cm and 20 cm the x-ray detectors were moved in 2.5-cm steps. Additional points were taken by moving the detectors back upstream in 2.5-cm steps with a 1.25-cm offset. The bi-directional scan tends to randomize long-term drift. Foil-detector separations in excess of 20 cm were reached by moving the foil upstream while the detectors were at their maximum

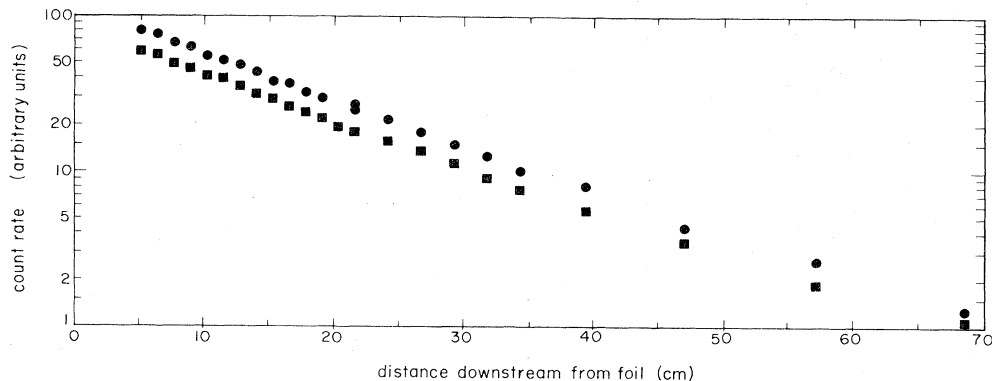


FIG. 14. Decay curves for the unperturbed  $2^2S_{1/2}$  state of hydrogenlike argon. The raw data are the counts in the 2.0–2.5 keV portion of the spectra shown in Figs. 6(a)–6(g) and other spectra. The circles are data from the detector located on the north side of the beam line (top x-ray detector in Fig. 3) and the squares are data from the south detector. Statistical error is roughly the size of the points.

downstream position (see Fig. 3).

The  $2^2S_{1/2}$  decay curves (Fig. 14) show very small background. After 4.9 mean lives, most of the counts still arise from the  $2^2S_{1/2}$  decay. From a least-squares fit to the decay curves of a single exponential plus a constant background we find backgrounds of 0.4% and 0.6% of the  $2E1$  amplitude (at  $t=0$ ) for the north and south detectors, respectively. We attribute the background, as opposed to the dead time, primarily to high-energy photons, Compton scattered in the detector. Small additional background arises from incomplete conversion<sup>23</sup> of x rays from the single-photon decays of hydrogenlike and heliumlike argon. In studies of background with the foil removed, we find no evidence of a position-dependent background.

After correcting for the 3.5% contribution from the heliumlike  $2^1S_0$  contaminant (section II B 12), the decay curves were fitted to a single exponential plus a constant background. The increase in the lifetimes due to subtracting out the heliumlike fraction was 1.4%

The (otherwise) uncorrected lifetimes from the least-squares fits to the two decay curves are nearly identical: 3.530(0.055) ns and 3.523(0.040) ns for the north and south detectors, respectively; where the errors are the uncertainty in the least-squares fit to the decay curve. Corrections to the measured lifetimes and systematic errors are tabulated in Table I. We correct for relativistic time dilation (0.9%), for collisional quenching (0.1%), for cascades (0.1%) and for dead time (0.2%). The total systematic error in the lifetime measurement from uncertainties in collisional quenching, cascades, the  $2^1S_0$  fraction, the beam velocity and dead time is 0.35%. Our final corrected value of the hydrogenlike argon  $2^2S_{1/2}$  lifetime is 3.487(0.036) ns.

### 16. Nonsingle exponential decays

Nonexponential decays characterized by higher decay rates at short times have been observed in the  $M1$  decay of

TABLE I. Contributions to the measured  $2^2S_{1/2}$  lifetime.

Uncorrected lifetime (ns)	3.479
Corrections (ns)	
collisional quenching	0.004
cascades	-0.004
$2^1S_0$ contamination	0.047
dead time	-0.007
time dilation	-0.032
Errors (ns)	
collisional quenching	0.004
cascades	0.004
$2^1S_0$ contamination	0.005
beam velocity	0.007
dead time	0.007
fitting	0.034
$2^2S_{1/2}$ lifetime (ns)	3.487 (0.036)

the  $2^3S_1$  state<sup>44–46</sup> of heliumlike argon, heliumlike chlorine, and heliumlike sulfur, and in the  $E1$  decay of the  $2^3P_0$  state of heliumlike argon.<sup>29</sup> The effect is significant at times shorter than 0.5 mean lives and cannot be explained by ordinary cascades to the  $2^3S_1$  and  $2^3P_0$  states. A possible explanation<sup>47</sup> of this phenomena is that the higher decay rate arises from unresolved lines from atoms with an additional electron in a state of high principle quantum number.

At present these effects have not been observed in hydrogenlike atoms. For example, studies<sup>48</sup> of the  $2^2S_{1/2}$  lifetime in hydrogenlike fluorine and hydrogenlike oxygen, performed under conditions virtually identical to those in Refs. 44–46 did not observe anomalously high decay rates.

A second electron could affect our measured  $2^2S_{1/2}$  state lifetime only under rather unlikely circumstances. The second electron initially would have to be in a long-lived state, which means a high- $n, l$  state. In a very-high- $n$  state, the second electron would interact weakly with the  $2s$  electron with little effect upon the  $2^2S_{1/2}$  lifetime. Before the  $2s$  electron decays, the second electron could decay to the  $1s$  state, or the atom could autoionize with the remaining electron decaying to the  $1^2S_{1/2}$  state. The result would then be a heliumlike atom in the  $2^3S_1$  or  $2^1S_0$  state or a hydrogenlike atom in the ground state. For this small population of atoms with one electron in the  $2s$  state and the other electron in a high- $n, l$  state one would measure a lifetime associated with the  $2E1$  decay rate of the  $2^2S_{1/2}$  state plus a decay rate characteristic of the cascade rate. This mechanism decreases the measured  $2^2S_{1/2}$  lifetime by an amount which depends upon the population of doubly excited heliumlike atoms.

The contribution of the doubly excited heliumlike atom to the measured lifetime can be estimated from the ratio of heliumlike to hydrogenlike argon in the beam and from the observed cascade rates to the  $2P$  states of hydrogenlike argon. From the data in Fig. 7(b) we found that the cascade rate in hydrogenlike argon was comparable to the  $M1$  decay rate, about 3% of the  $2E1$  rate. Since the ratio of hydrogenlike argon to heliumlike argon in the beam is 16 to 1, we take the heliumlike cascade rate to be roughly  $2 \times 10^{-3}$  of the  $2E1$  rate. Were every highly excited heliumlike atom to be doubly excited with one electron in the  $2s$  state then our apparent  $2^2S_{1/2}$  lifetime would be shortened by about 0.1%. The models of cascade feeding in Ref. 33 use population distributions which scale as  $n^{-3}$ . In this distribution only 1/8 of the highly excited heliumlike atoms will have the other electron in the  $n=2$  state, and only a fraction of those in the  $2s$  state. (In hydrogenlike argon we find that some 3% of the atoms are formed in the  $2^2S_{1/2}$  state.) Our estimate is that the  $2s$ , high- $n, l$  atoms shorten the apparent  $2^2S_{1/2}$  lifetime by only 0.01%.

To test for this effect in the decay of the  $2^2S_{1/2}$  state of hydrogenlike argon, we repeated the least squares fits to the decay curves after removing data points from successively larger distances downstream from the foil. Figure 15 shows a graph of the mean life as a function of the minimum distance downstream from the foil. Any change in the lifetime is considerably smaller than the er-

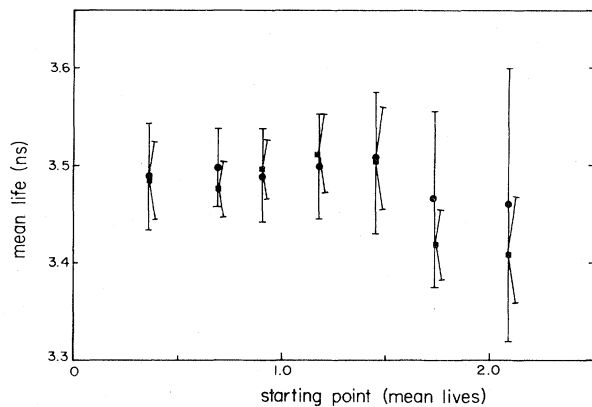


FIG. 15. Measured  $2^2S_{1/2}$  lifetime in hydrogenlike argon as a function of the distance downstream from the foil of the first point on the decay curve. Refitting to the decay curve after deleting data from small distances downstream from the foil is a test of the single exponential character of the decay curve.

ror in the fit to the original decay curve and the result is consistent with there being no effect.

### C. Comparison with theory

Our value of 3.487(0.036) ns for the lifetime of the  $2^2S_{1/2}$  state of hydrogenlike argon is in agreement with the theoretical value of 3.497 ns obtained from the  $2E1$  decay rate calculated by Goldman and Drake<sup>2</sup> plus the  $M1$  decay rate calculated by Johnson,<sup>3</sup> and Parpia and Johnson,<sup>4</sup> as well as the  $2E1$  plus  $M1$  decay rates calculated by Parpia and Johnson.<sup>4</sup> Our value is also in agreement with the earlier measurement of Marrus and Schmieder<sup>15,37</sup> of 3.5(0.25) ns. As the  $M1$  decay contributes 3.2% to the total decay rate our measurement is sensitive to its presence. The relativistic corrections of 1.1% to the  $2E1$  decay rate are the same size as the experimental uncertainty. Measurements of the lifetime of the  $2^2S_{1/2}$  state in the hydrogen isoelectronic sequence are tabulated in Fig. 16. Agreement with theory is uniformly good.

$$F(Z\alpha) = [A_{40} + A_{41} \ln(Z\alpha)^{-2} + A_{50}(Z\alpha) + A_{60}(Z\alpha)^2 + A_{61}(Z\alpha)^2 \ln(Z\alpha)^{-2} + A_{62}(Z\alpha)^2 \ln^2(Z\alpha)^{-2} + A_{70}(Z\alpha)^3 + \dots]. \quad (2)$$

Values of the coefficients (which are weakly dependent upon  $n$ ) can be found in Refs. 54–57 and values for the  $1^2S_{1/2}$  state are summarized in Ref. 58.

The relative importance of the higher-order terms at  $Z=18$  can be seen by comparing values of different terms at  $Z=1$  and  $Z=18$ . The terms of order  $\alpha(Z\alpha)^6$ , (coefficients  $A_{60,61,62}$ ) which contribute 0.016% of the Lamb shift in hydrogen give 12% of the Lamb shift at  $Z=18$ .

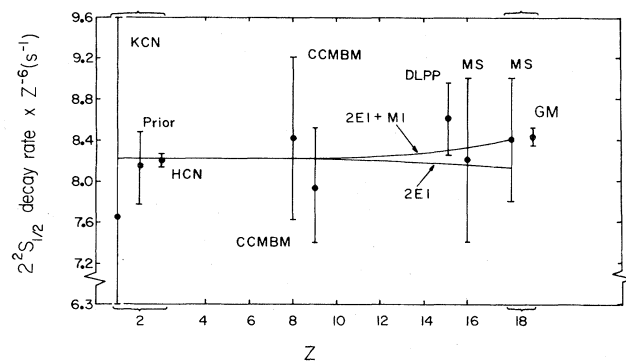


FIG. 16. Comparison of experimental and theoretical  $2^2S_{1/2}$  decay rates of the hydrogen isoelectronic sequence. All decay rates have been divided by  $Z^6$ . Theory is from Refs. 2–4 and 10. The nonrelativistic  $2E1$  decay rate is  $8.229 Z^6$ ; and the relative decrease in the theoretical  $2E1$  rate with increasing  $Z$  is due to the relativistic correction. The  $M1$  rate which scales roughly as  $Z^{10}$  is included in the upper curve. The references associated with the experimental points are as follows: GM—this work, MS—Ref. 15, CCMBM—Ref. 48, DLPP—Ref. 49, HCN—Ref. 50, Prior—Ref. 51, and KCN—Ref. 52.

## III. LAMB SHIFT IN HYDROGENLIKE ARGON

### A. Theory

The availability of precise and unambiguous calculations of the  $2^2S_{1/2}$ - $2^2P_{1/2}$  energy splitting (Lamb shift) in the hydrogen isoelectronic sequence makes the comparison between Lamb-shift theory and experiment in a high-nuclear-charge  $Z$  hydrogenlike atom a rigorous test of quantum electrodynamics (QED) in strong fields. At high  $Z$ , where the binding energy of the electron becomes an appreciable fraction of its rest mass, the higher-order terms in the QED correction to the binding energy become relatively more important.<sup>53</sup>

For  $Z < 137$  the largest contribution to the Lamb shift is the self-energy  $\Sigma_n$ :

$$\Sigma_n = n^{-3} (\alpha/\pi)(Z\alpha)^4 F(Z\alpha) m_e c^2 \quad (1)$$

where  $\alpha$  is the fine-structure constant,  $Z$  the nuclear charge,  $n$  the principle quantum number, and  $m_e$  the electron rest mass.  $F(Z\alpha)$  can be represented as a power series in  $\alpha$  and  $Z\alpha$ :

The term of order  $\alpha(Z\alpha)^7$ , (coefficient  $A_{70}$ ) contributes only  $1.5 \times 10^{-7}$  of the Lamb shift at  $Z=1$ , but gives 2.5% of the Lamb shift at  $Z=18$ . This term is presently tested only in this experiment and in Lamb-shift measurements at  $Z=17$  (Ref. 59) and  $Z=15$  (Ref. 60). Terms of order  $\alpha(Z\alpha)^6$  are tested to roughly comparable accuracy in our Lamb-shift measurement and in a number of Lamb-shift measurements at lower  $Z$ .

Although additional terms of order  $\alpha(Z\alpha)^7$  and higher-order terms have not been calculated explicitly, techniques have been developed to obtain the complete self-energy. Erickson<sup>56</sup> has used an analytic approximation to obtain values of the self-energy for all  $Z$ ; and Mohr<sup>58,61,62</sup>, using Coulomb radial Green's functions, has obtained an expression for the self-energy which can be numerically integrated for  $Z$  between 10 and 110.

When combined<sup>53,62</sup> with the vacuum polarization<sup>63</sup> ( $-2.6$  THz), the fourth-order correction<sup>64</sup> (0.01 THz), and the reduced mass, relativistic recoil, and nuclear size corrections<sup>53,62</sup> (a total of 0.29 THz), Mohr<sup>62</sup> obtains a value of the Lamb shift of hydrogenlike argon of  $S = 38.25(0.025)$  THz, while Erickson<sup>14,56</sup> using similar values for the vacuum polarization, etc., obtains a Lamb shift of  $S = 39.0(0.16)$  THz.

### B. Electric field quenching of the $2^2S_{1/2}$ state

In the presence of an external electric field, the  $2^2S_{1/2}$  state wave function becomes a mixture of the unperturbed  $2^2S_{1/2}$  and  $2^2P_{1/2}$  state eigenfunctions<sup>65</sup> and to some extent, all other  $nP$  states. As the  $nP$  states have large single-photon  $E1$  decay rates to the ground state, the lifetime of the perturbed  $2^2S_{1/2}$  state is shortened (quenched). The quenched  $2^2S_{1/2}$  state will decay by  $E1$  as well as  $2E1$  and  $M1$  radiation. In hydrogenlike argon, an electric field of  $6.5 \times 10^5$  V/cm induces an  $E1$  decay rate of  $2.9 \times 10^8$  s<sup>-1</sup>, equal to the (natural)  $2E1$  decay rate of the  $2^2S_{1/2}$  state.

If the perturbation of the energy levels by the electric field is sufficiently small compared to the Lamb shift ( $E \ll 100Z^5$  where  $E$  is in V/cm), then the mixing with the  $n > 2$   $nP$  eigenfunctions can be neglected. The lowest-order quenched decay rate for the  $2^2S_{1/2}$  state,  $R_S$  becomes<sup>66,67</sup>

$$R_S = \Gamma_S + \frac{\left[ V_{ps} \right]^2 \Gamma_p}{\hbar \left[ \omega_s^2 + \frac{1}{4} \Gamma_p^2 \right]} + \frac{\left[ V_{qs} \right]^2 \Gamma_q}{\hbar \left[ (\omega_{pq} - \omega_s)^2 + \frac{1}{4} \Gamma_q^2 \right]}, \quad (3)$$

where  $\hbar$  is Planck's constant divided by  $2\pi$ ,  $\Gamma_S$ ,  $\Gamma_p$ , and  $\Gamma_q$  are the natural decay rates of the  $2^2S_{1/2}$ ,  $2^2P_{1/2}$  and  $2^2P_{3/2}$  states in units of s<sup>-1</sup>; and  $\omega_s$  and  $\omega_{pq}$  are the Lamb shift and the  $2^2P_{1/2}$ - $2^2P_{3/2}$  fine-structure splitting in units of radians/s.  $V_{ps}$  and  $V_{qs}$  are the electric-dipole matrix elements between the  $2^2S_{1/2}$  and  $2^2P_{1/2}$  states and between the  $2^2S_{1/2}$  and  $2^2P_{3/2}$  states, respectively. The last term in Eq. (3) is the decay rate induced by the mixing of the  $2^2P_{3/2}$  state. In hydrogenlike argon  $\omega_{pq} = 7.31620(0.0006) \times 10^{15}$  radians/s<sup>14</sup> (versus  $2.38 \times 10^{14}$  radians/s for the Lamb shift), hence this term contributes less than 0.1% to the quenched decay rate.

$\Gamma_S$  is, from this experiment,  $2.868(0.03) \times 10^8$  s<sup>-1</sup> and from theory<sup>2,4</sup>  $2.860 \times 10^8$  s<sup>-1</sup>. The  $2^2P_{1/2}$  and  $2^2P_{3/2}$  states (Fig. 1) decay to the ground state by allowed electric-dipole decay with rates<sup>66</sup> of  $6.591 \times 10^{13}$  s<sup>-1</sup> and

$6.552 \times 10^{13}$  s<sup>-1</sup>, respectively. The faster decay rate for the  $2^2P_{1/2}$  state is due to different relativistic corrections in the electric-dipole matrix elements of the  $2^2P_{1/2}$  and  $2^2P_{3/2}$  states. The  $2^2P_{3/2}$  state also decays to the ground state by magnetic-quadrupole ( $M2$ ) decay, to the  $2^2P_{1/2}$  state by  $M1$  decay and to the  $2^2S_{1/2}$  state by allowed  $E1$  decay. In hydrogenlike argon all of these decay rates are calculated to be less than  $10^{-5}$  of the  $E1$  rate to the ground state.

Electric-dipole matrix elements  $V_{ps}$  and  $V_{qs}$  including relativistic corrections have been calculated by Hillery and Mohr.<sup>66</sup> They are

$$V_{ps} = -eEa_0(\sqrt{3}/Z)[1 - 0.4167(Z\alpha)^2 F_5(Z\alpha)] \quad (4)$$

and

$$V_{qs} = -eEa_0(\sqrt{6}/Z)[1 - 0.1667(Z\alpha)^2 F_6(Z\alpha)]. \quad (5)$$

Where  $\alpha$  is the fine-structure constant,  $e$  is the electron charge in esu, and  $E$  is the electric field in statvolts/cm. From Figs. 4 and 5 of Ref. 66 we obtain  $F_5 = 1.003$  and  $F_6 = 1.007$ . The quantity  $[ -0.4167(Z\alpha)^2 F_5(Z\alpha) ]$  is the relativistic correction to  $V_{ps}$ . At  $Z = 18$ , the relativistic correction reduces the quenched  $E1$  decay rate by 1.4%.

The electric-field-induced splitting of the  $2^2S_{1/2}$  and  $2^2P_{1/2}$  states is of order  $V_{ps}/\omega_s = V_{ps}^2 \Gamma_p \omega_s / \omega_s^2 \Gamma_p$ . The quantity  $V_{ps}^2 \Gamma_p / \omega_s$  is roughly the quenched  $E1$  decay rate ( $R_{QD}$ ). The induced splitting is then  $\omega_s \times R_{QD} / \Gamma_p$ . In an electric field of  $6.5 \times 10^5$  V/cm,  $R_{QD} / \Gamma_p \approx 5 \times 10^{-6}$  and the increase in the  $2^2S_{1/2}$ - $2^2P_{1/2}$  splitting is of order  $10^{-5}$  of the Lamb shift.

As yet no effect of an electric field on the angular distribution of the two-photon electric-dipole radiation has been observed or calculated. The angular distribution of the quench radiation<sup>66,68-70</sup> exhibits an anisotropy and an asymmetry with respect to the direction of the electric field. The anisotropy, and a polarization effect, arise from interference in the mixing of the  $2^2P_{1/2}$  and  $2^2P_{3/2}$  eigenfunctions with the  $2^2S_{1/2}$  eigenfunction. The asymmetry, and again a polarization effect, arise from interference between the induced  $E1$  decay and the spontaneous  $M1$  decay of the  $2^2S_{1/2}$  state.

### C. Experimental studies of the Lamb shift in hydrogenlike argon

#### 1. Production of electric fields

A uniform electric field in the rest frame of the atom is produced by passing the beam of atoms through a homogeneous magnetic field. At the maximum magnetic field of 2.13 T used in our experiment, the electric field in the rest frame of the argon beam traveling at  $4 \times 10^9$  cm/s ( $\beta = v/c = 0.134$ ), is  $\vec{E} = \gamma(v/c) \times \vec{B} = 2.88 \times 10^3$  statvolt/cm ( $8.65 \times 10^5$  V/cm). The determination of the Lamb shift by Eqs.(3)–(5) requires the simultaneous measurement of three quantities: the magnetic field, the beam velocity, and the decay length of the quenched  $2^2S_{1/2}$  state.

*a. Zeeman effect.* The magnetic field also Zeeman

splits the  $m_j$  levels of the fine-structure states according to the quantum numbers  $l, j$ , and  $m_j$ . There is no hyperfine structure in the even mass isotopes of argon which account for 100% of the naturally occurring element. The  $m_j = 1/2, -1/2$  splitting is 28 GHz/T in the  $2^2S_{1/2}$  state of a hydrogenlike atom, and 9.3 GHz/T in the  $2^2P_{1/2}$  state. For Zeeman splittings which are much smaller than the Lamb shift, the  $2^2S_{1/2}$ - $2^2P_{1/2}$  splitting, averaged over both  $m_j$  levels remains unchanged. The difference in  $2^2S_{1/2}$ - $2^2P_{1/2}$  splittings for the different  $m_j$  levels produces a difference in quenching rates for the two levels, and a small change in the overall quench rate. The quench rate scales as  $(\Delta W/\omega_s)^2$  where  $\omega_s$  is the  $2^2S_{1/2}$ - $2^2P_{1/2}$  splitting and  $\Delta W$  is the Zeeman splitting. In a field of 2 T the Zeeman splittings of the  $2^2S_{1/2}$  and  $2^2P_{1/2}$  states of hydrogenlike argon are 0.074% and 0.025% of the Lamb shift. The difference in quench rates is therefore not significant in our experiment.

*b. Measurement of the magnetic field.* The magnetic field is measured with an integrating flux magnetometer,<sup>71</sup> which works by integrating the voltage generated by the change in the magnetic flux intersecting an approximately 5000-turn coil<sup>72</sup> of 1-cm diameter. We compensate for drift in an amplifier and the integrator by comparing the integrated voltage from the coil with the integrated voltage from a precision flux generator producing a constant fraction of a volt second. The flux generator<sup>72</sup> consists of a temperature-controlled toroidal transformer which is driven to saturation and then reversed.

Because the magnetometer measures changes in the magnetic field it is an excellent instrument for mapping the magnetic field homogeneity. We measure the absolute fields by rotating the coil through 360 degrees and recording the maximum swing in the integrated voltage. The maximum swing is the flux change corresponding to twice the magnitude of the magnetic field. An alternate method is to orient the coil in the magnetic field so as to produce the largest absolute reading and then return it to a field-free region. Both methods are used and give identical results.

The magnetometer and flux generator were calibrated against a nuclear-magnetic-resonance Gaussmeter at magnetic fields of 2.03, 1.87, 1.77, 1.66, and 0.66 T in the same magnet as used for the Lamb-shift measurement. We take as the calibration uncertainty 0.03%; the largest calibration difference between any two fields (in this case 0.66 T and 1.87 T). At least two measurements were made for each magnetic field during an experiment. In all cases the measurements agreed to better than 0.05%. Our total uncertainty in the absolute field, mainly due to drift in the electronics, is less than 0.05%.

We made radial and azimuthal field maps, including fringing fields, at each of the four fields, 2.133, 1.999, 1.768, and 1.472 T used in the Lamb-shift experiment. This was done to provide the data to calculate the beam trajectory, which is used to correct for changes in x-ray intensity due to deflection of the beam by the magnetic field, as well as to ensure that the fields were homogeneous over the measurement region. Radial maps of the magnetic field were made by moving the magnetometer coil along a track which went through the geometric center of the

magnet. The track was rotated to obtain the azimuthal dependence of the field and to determine the relation between the geometric and magnetic centers of the magnet. Measurements of the magnetic field outside of the homogeneous region of the magnet were made in step sizes of one percent or less of the central field. The region of the magnetic field used in measuring the quenched  $2^2S_{1/2}$  decay length has a homogeneity of better than 99.9% over a circular volume 25 cm in diameter by 2 cm high. We obtained this homogeneity in a magnet with 34-cm-diameter pole tips and a 6-cm gap by using a different set of magnetic shims for each of the three highest fields. The magnet pole tips and shims were built from a design, by Halbach and Magyary,<sup>74</sup> based upon a general purpose program for inversion system analysis.

The magnetic fields were set by slowly raising the magnetic field to saturation at about 2.3 T and then slowly lowering the field to its final value. This procedure gave magnetic field distributions, independent of the previous history of the magnet and the shims, independent of polarity, and reproducible to within the sensitivity of the magnetometer.

## 2. Changes in count rate due to beam dynamics

Ar<sup>17+</sup> ions traveling at  $4 \times 10^9$  cm/s in a 2-T field follow a circular trajectory with a 0.5-m radius. The complete trajectory of the beam through the magnet is shown in Fig. 17.

A change in the intensity seen by the x-ray detectors, of the x rays emitted by the argon ions arises from the displacement of the beam, from the change in orientation of the beam, and from the change in the direction of travel of the beam.

The effect of the beam displacement is to change the solid angle and the length of the beam viewed by the x-ray detectors. Because the distance between the detectors and the beam trajectory is large compared to the displacement of the beam, the change in solid angle and field of view of the detectors changes the intensity by only about 10% over a 20-cm decay curve.

The change in orientation of the beam away from the normal to the line of sight of the x-ray detectors allows the detectors to observe longer segments of the beam. For small angles of beam deflection  $\theta$ , the effect scales roughly as  $1/\cos\theta$ ; always increases the observed intensity, and exceeds 20% at the largest deflections in our experiment. The curved trajectory of the beam also causes its path length through the measurement region to increase. Values of the beam path length versus the position of the x-ray detector viewing the beam are tabulated in Table II.

Two effects which are related to the beam velocity, as well as the beam trajectory, are the Doppler shift and the intensity change due to radiation anisotropy. The radiation anisotropy is due to the fact that the angular distribution of radiation from a moving object, which is isotropic in its rest frame, is not isotropic when seen in the laboratory frame. The trajectory of the beam, shown in Fig. 17, results in different angles of observation at different detec-

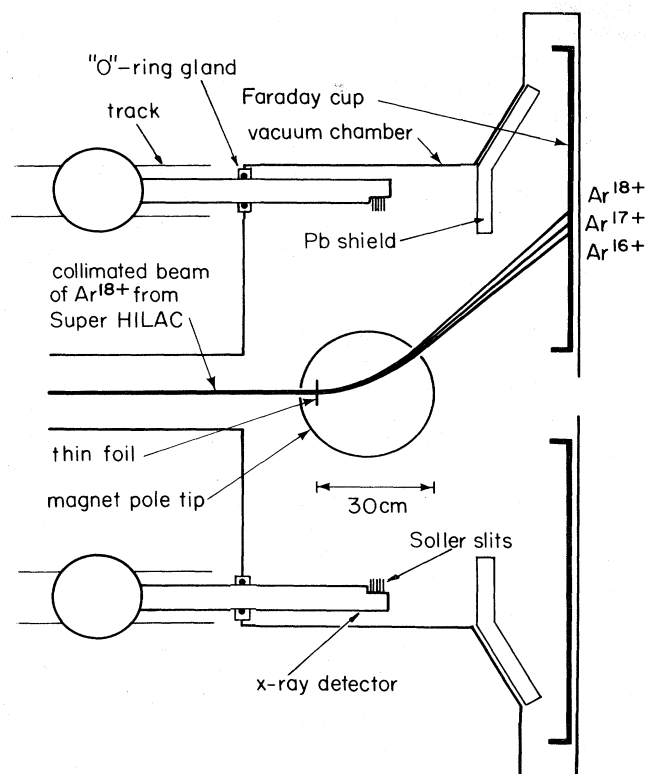


FIG. 17. Schematic diagram of the apparatus used to measure the lifetime of the quenched  $2^2S_{1/2}$  state of hydrogenlike argon. The trajectory shown is for a beam of argon ions traveling at  $4 \times 10^9$  cm/s through a magnetic field of 2.0 T. At this field our magnet has an effective radius of 22.5 cm.

tor positions. The intensity as a function of angle has been calculated by Weisskopf.<sup>75</sup> If  $I(\theta)$  and  $I_0(\theta')$  are the angular distributions of the radiation in the rest frames of the laboratory and the moving system, respectively, then

$$K(\theta) = \frac{I(\theta)}{I_0(\theta')} = \frac{1 - \beta^2}{(1 + \beta \cos \theta)^2} \quad (6)$$

where  $\beta = v/c$  and  $\theta$  is the angle of observation with  $\theta = \pi/2$  being the forward direction of the beam. The intensity of the radiation as a function of angle, viewed in the the laboratory frame, for a source which radiates isotropically in its rest frame moving at  $4 \times 10^9$  cm/s ( $\beta = 0.134$ ) is shown in Fig. 18, and values of  $K(\theta)$  for this experiment are listed in Table II.

The Doppler shift is given by:  $\omega = \omega_0 K^{1/2}(\theta)$  where  $\omega$  and  $\omega_0$  are the x-ray energies in the laboratory frame and the rest frame of the argon beam, respectively, and  $K(\theta)$  is defined by Eq.(6). The Doppler shift has a small effect on the measured x-ray intensity because the efficiency of the x-ray detectors is energy dependent. A model for this correction is presented in section III C 5.

### 3. A model for calculating changes in the intensity

To perform detailed calculations of the change in the x-ray intensity seen by the x-ray detectors we constructed a numerical model for the trajectory of the beam and for the optics of the x-ray detectors. The beam trajectory in the magnetic field and the components of velocity are calculated in small increments of time by repeated application of Newton's law. The input data for the beam trajectory are the radial and axial maps of the magnetic field, the location of the foil where the charge state changes from  $18+$  to  $17+$ , and the measured beam velocity.

We treat each increment along the trajectory as a fixed, isotropically radiating point source. For each position of the x-ray detector, we calculate the solid angle occupied by the detector which is illuminated through the detector collimating slits by each of the point sources. The sum of the solid-angle contributions from all of the point sources is the relative intensity seen at each detector position. With increasing beam deflection a larger number of point

TABLE II. Calculated changes in the observed x-ray intensity due to deflection of the beam in a magnetic field of 1.998 T.

Foil-detector separation <sup>a</sup> (cm)	Beam path length <sup>b</sup> (cm)	Geometry correction <sup>c</sup>		Angle (rad)	Anisotropy correction <sup>d</sup>
		Towards	Away		
5.03	5.15	1.067	0.981	0.264	1.055
7.56	7.79	1.100	0.984	0.318	1.070
10.10	10.49	1.142	0.988	0.372	1.086
12.65	13.26	1.195	0.933	0.428	1.102
15.18	16.07	1.260	1.003	0.485	1.118
17.73	19.00	1.343	1.010	0.544	1.134
20.28	22.04	1.449	1.024	0.605	1.151

<sup>a</sup>Distance of x-ray detectors downstream from the foil.

<sup>b</sup>Path length of the beam with the foil at  $l=0$ .

<sup>c</sup>The correction for the change in solid angle and the length of beam viewed relative to the solid angle and length of beam viewed at the foil. Toward (away) refers to a beam bent towards (away from) the x-ray detector.

<sup>d</sup>Anisotropy correction for a beam bent toward the x-ray detector. The anisotropy correction for a beam bent away from the detector is  $0.982/K$ , where  $K$  is the correction for the beam bent towards the detector. The factor of 0.982 is the relativistic contribution to the anisotropy.

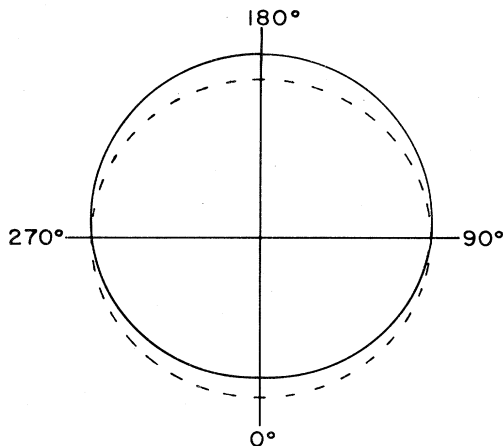


FIG. 18. Polar map of the intensity of radiation in the laboratory frame from a source which radiates isotropically in its own reference frame moving at  $4 \times 10^9$  cm/s.

sources contributes to the intensity. The number of time-increment steps required for the beam to be seen by the x-ray detector in different positions divided by the time per increment determines the distance traveled by the beam. Finally, the radiation anisotropy is calculated from Eq.(6) with velocity components obtained from the trajectory calculation.

The precision of the model depends upon knowledge of the magnetic field distribution, the position response of the x-ray detectors, and the locations of the x-ray detectors and the foil. The magnetic field mapping was described in section III C 1b.

The x-ray detectors are collimated by Soller slits<sup>24</sup> mounted on rocker arms attached to the x-ray detectors. The slits are 2 cm deep with 0.7-mm-wide openings spaced every 1.0 mm for 12 mm. By sighting a telescope through holes in the magnet yoke and vacuum chamber we adjust the rocker arms so that the view of the x-ray detectors is normal to the axis of the beam line to within a few milliradians.

We determined the position response of each x-ray detector by translating the x-ray detector past a collimated x-ray source located 0.6 m away on the beam axis. The x-ray source is  $^{55}\text{Fe}$  whose decay by electron capture produces manganese  $K_\alpha$  and  $K_\beta$  x rays at 5.9 keV and 6.5 keV, respectively. The response pattern of the collimated x-ray detector to the collimated x-ray source is a nearly perfect isosceles triangle with base of 3.6 cm for the north detector and 4.1 cm for the south detector. The differences in the response are due to variations in the active area of the detectors, and the spacing of the collimator from the x-ray detector. We adjusted our model to account for the differences and obtained a calculated response which was within a few percent of measurements. The differences in the optics of the two detectors made only minor differences in the intensity corrections.

We measured the positions of the x-ray detectors, the foil and other mechanical components relative to the center of the magnet by a series of mechanical and optical measurements referenced to the center of the magnet. The

calibration for x-ray detector location was taken from its position response after determining the location of the x-ray source relative to the center of the magnet. To discourage misalignment of the apparatus by geological activity, the x-ray detectors were clamped to a track which in turn was secured to a rigid table attached to the magnet yoke. The vacuum chamber was pinned to the magnet yoke, and the magnet and the vacuum boxes which held the beam collimators were fastened to the 15-cm-thick reinforced concrete floor.

#### 4. A test of the model

We tested our calculation by observing the 3.10-keV x ray from the 208-ns magnetic-dipole decay<sup>21</sup> of the  $2^3S_1$  state of heliumlike  $\text{Ar}^{16+}$ . We used the same beam velocity as for hydrogenlike  $\text{Ar}^{17+}$ , but the magnetic fields were increased to produce roughly the same trajectory. As the  $2^3S_1$  state of heliumlike argon is not quenched in the 2-T magnetic field, its roughly 8-m decay length means that changes in the 3.1-keV x-ray intensity are primarily due to trajectory effects.

The  $2^3S_1$  state was prepared by stripping an  $\text{Ar}^{13+}$  beam from the Super-HILAC in a  $50\text{-}\mu\text{g}/\text{cm}^2$  carbon foil located three meters upstream from the magnet. Placing the foil far upstream allows the shorter-lived states and cascades to depopulate. We measured intensity versus detector position at 4 magnetic fields, chosen to most nearly duplicate the trajectory of the heliumlike argon beams in our Lamb-shift measurements.

Figures 19(a) and 19(b) show the observed count rate in two detectors from the decay of the  $2^3S_1$  in a magnetic field of 1.92 T. Also shown is the count rate corrected by our model for geometrical effects and anisotropy. The correction for detector efficiency which changes by less than two percent from the smallest to the largest deflection is included in Figs. 19(a) and 19(b). The consistency of the corrected count rates indicates that no important effects have been neglected in our analysis.

#### 5. Correction for Doppler shifts

In addition to the geometrical and anisotropy corrections, we apply two Doppler-shift corrections to the electric-field-quenched two-photon spectra. First, we adjust the wavelength region of the observed spectra used to determine the quenched  $2^2S_{1/2}$  count rate so that it corresponds to x rays emitted at energies from 2.0 keV to 2.5 keV in the rest frame of the  $\text{Ar}^{17+}$  beam. Second, we correct for the change in efficiency of detecting the Doppler-shifted x ray. At 2.3 keV, the x-ray detector efficiency changes by about three percent over a typical decay curve in which the Doppler shift spans 100 eV.

The x-ray detector efficiency, or more precisely its spectral response, is largely determined by photoelectric absorption of the x rays before they reach the active portion of the detector. Other effects which influence the spectral response are fluorescence x rays and Auger electrons produced outside the active region, and incomplete conversion of x rays inside the active area.

On top of the active area of each detector is an inactive

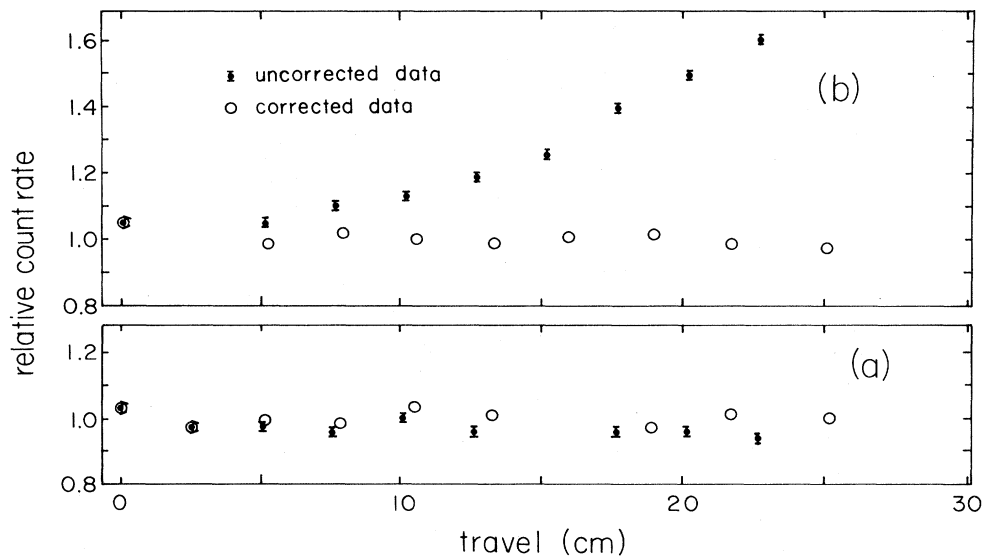


FIG. 19. (a),(b) Decay curves from the decay of heliumlike  $2^3S_1$  in magnetic field of 1.92 T; in (a) the beam is deflected away from the x-ray detector and in (b) it is deflected towards. The decay length of the  $2^3S_1$  state is over 8 m and the change in count rate is almost entirely due to deflection of the beam in the magnetic field. Figures (a) and (b) show the decay curves from the uncorrected count rate, and the count rate corrected for beam displacement, the change in the orientation of the beam, radiation anisotropy, and detector efficiency. In addition, the corrected points are displaced along the axis due to a correction for total beam travel.

silicon layer approximately 200 nm thick. Evaporated onto the silicon is a gold conductive coating with an effective thickness of about 8 nm. This detector element then sits behind a 0.01-mm-thick beryllium window; part of a vacuum enclosure which isolates the liquid-nitrogen-cooled detector from outside contamination. The energy-dependent x-ray transmission of these individual components, based upon a determination of their thickness and the cross sections in Ref. 25, is shown in Fig. 20 and the total transmission is shown in Fig. 4.

We determine the thickness of the inactive silicon layer by observing low-energy bremsstrahlung continuum and comparing the change in x-ray intensity at the silicon  $K$  edge of 1.84 keV with the change in cross section in Ref.

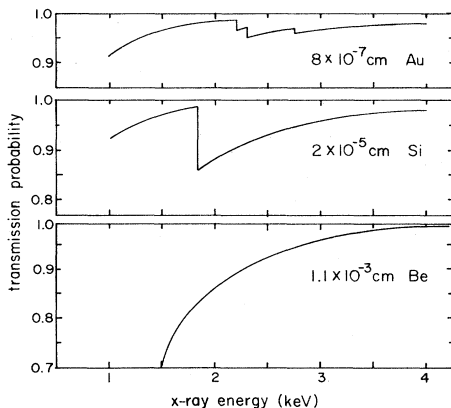


FIG. 20. Transmission, as a function of x-ray energy, through the materials covering the active portion of the x-ray detector. The combined transmission is shown in Fig. 4.

25. This yields a thickness of 200(40) nm, in agreement with a value of 200 nm in similar detectors determined by Pehl *et al.*<sup>43</sup> from measurements of energy loss by  $\alpha$  particles as a function of angle.

The deposited gold which forms the conductive layer has an estimated thickness<sup>76</sup> of 20 nm, but electron microscope studies find that half or more of the detector area remains uncoated<sup>76</sup>. An effective value of 8 nm for the thickness of the gold layer is not inconsistent with our observations of the bremsstrahlung spectrum.

An average beryllium thickness of  $1.0 \times 10^4$  nm was determined by weighing the window prior to assembly. Beryllium foils typically contain about 1.5% impurity by weight of which 80% is BeO and the rest is Mg, Al, Si, Fe, and their compounds. The high- $Z$  impurities, particularly the Fe add about 20% to the effective thickness of the beryllium window in the 2.0-keV to 2.5-keV region.

From the product of the transmissions of the components, we find that the change in the x-ray detector efficiency in the 2.0-keV to 2.5-keV region averages 0.7% for every 1% change in x-ray energy; or 3.2% for a 100-eV change. Uncertainty in the thickness of the window materials causes an uncertainty in the slope of the transmission versus energy curve and in turn in the energy-dependent correction. We estimate the uncertainties in the thickness of the beryllium window and in the inactive silicon layer each to be 20% and the uncertainty in the effective thickness of the gold layer to be 50%. This results in an uncertainty of less than 0.6% in the change in the transmission for a 100-eV Doppler shift. The dominant contribution of 0.5% to this uncertainty is the uncertainty in the thickness of the beryllium window. For a typical quenched  $2^2S_{1/2}$  decay curve of three decay lengths and a Doppler shift spanning 100 eV, the transmission uncer-

tainty introduces an error into the measured decay length of roughly 0.2%. The change in window transmission is fairly linear above 2.0 keV so that almost all of the error cancels when averaging decay lengths measured with opposing x-ray detectors.

In addition to photoelectric absorption and a small amount of Compton scattering, there are effects due to fluorescence in gold and silicon, and Auger electrons produced in the dead layer. X rays at energies above 1.84 keV absorbed in the silicon dead layer produce  $K$  vacancies, of which some 95% fill by Auger emission. The Auger electrons with a maximum energy of 1.83 keV lose energy at a rate<sup>77</sup> of 15 eV/nm so that electrons which reach the active portion of the detector usually have little remaining energy. The other 5% of the  $K$  vacancies are filled by radiative decay with emission of a  $K\alpha$  or  $K\beta$  x ray at 1.74 keV or 1.83 keV, respectively. The instrumental linewidth of the x-ray detector is sufficiently broad so that a tail from the 1.83-keV line extends beyond 2.0 keV. A small correction is made for this effect.

$M$ -shell vacancies produced in the gold fill predominantly by radiative decay producing 8 lines in the 1.7-keV to 2.9-keV region. We estimate the strength of these lines from the height of the absorption edges<sup>25</sup> associated with the onset of vacancy production. The contribution to the 2.0-keV to 2.5-keV portion of the spectra from gold fluoresced by x rays over our one-photon and two-photon spectra is about 1 part in 500 and changes only slightly for Doppler shifted spectra.

The final contribution to the spectral response of the x-ray detector efficiency which we consider involves the active portion of the detector. The 1.74-keV (or the weaker 1.83 keV) x ray from radiative decay of the silicon  $K$  vacancy can escape the detector. This results in an escape peak in that the measured x-ray line is 1.74 keV below the incident x-ray energy. As higher-energy photons are, on average, absorbed deeper in the detector the escape probability decreases for higher-energy x rays. This energy-dependent escape probability for a silicon detector has been measured by Woldseth<sup>78</sup> who finds for 2.5-keV x rays the escape probability is 1.5% with a slope of -0.02% per 1% change in energy. Although included in our energy dependent correction, these effects are small and their influence upon the measured  $2^2S_{1/2}$  quenched decay length is insignificant.

### 6. Observation of the quench spectra

Figures 21(a)–21(d) show the spectra from the decays in flight of the hydrogenlike argon and the small heliumlike argon contaminant, in a motional electric field of  $7.14 \times 10^5$  V/cm. The ratio of intensity of the single photon peak to the two-photon continuum is enhanced by the electric field quenched decay of the  $2^2S_{1/2}$  state. Due to the Doppler shift the peaks in Figs. 21(a)–21(d) are slightly displaced from each other and from the peaks in the spectra of the unperturbed decay in Figs. 6(a)–6(g). Aside from the Doppler shift, the shape of the two-photon continuum is unchanged.

Fitting the x-ray detector line shape (as in section II B 6) to the single-photon peaks in the spectra of the decays in a

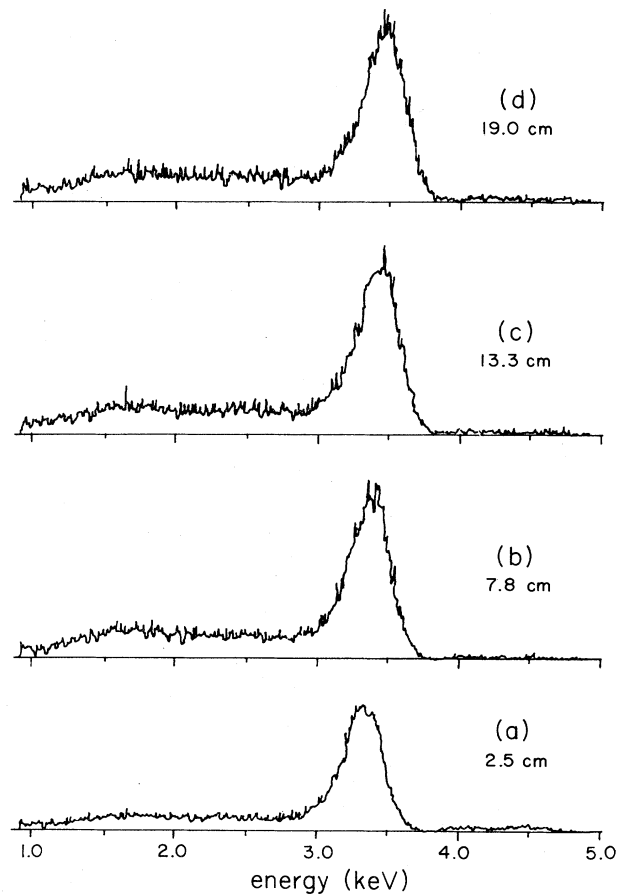


FIG. 21. (a)–(d). Observed spectra from the decays in flight of hydrogenlike argon (and a small amount of heliumlike argon) in a motional electric field of  $7.14 \times 10^5$  V/cm, as a function of distance downstream from the foil. The displacement of the peaks is due to the Doppler shift as the beam is deflected toward the x-ray detector.

field of  $7.14 \times 10^5$  V/cm (a magnetic field of 1.77 T) and correcting for Doppler shift, we find the hydrogenlike component at 3314(13) eV and a small heliumlike component at 3118(24) eV. The errors are the standard deviation of the mean energy from fits to 70 spectra from two detectors, combined with a 10-eV calibration uncertainty. (The calibration is against the 6.898-keV manganese  $K$  x ray from an  $^{55}\text{Fe}$  source.) These energies are in agreement with the theoretical transition energies<sup>14,27</sup> of 3318 eV for the decay of the  $2^2S_{1/2}$  and  $2^2P_{1/2}$  states, and 3323 eV for the decay of the  $2^2P_{3/2}$  state to the ground state in hydrogenlike argon; and 3122 eV and 3104 eV for the decay of the  $2^3P_2$  and  $2^3S_1$  states to the ground state in heliumlike argon.

Although most of the counts in the hydrogenlike peak arise from the quenched decay of the  $2^2S_{1/2}$  state, an estimated 6% of the counts in the peak still arise from cascades to the  $2P$  states. For this reason we construct the decay curves to determine the quenched  $2^2S_{1/2}$  lifetime from the two-photon continuum spectra.

### 7. Quenched $2^2S_{1/2}$ state decay curves

Lifetimes of the quenched  $2^2S_{1/2}$  state were measured over an average of 2.5 decay lengths in electric fields of plus and minus (5.93, 7.14, 8.06, and 8.60)  $\times 10^5$  V/cm with two detectors for a total of sixteen decay curves. At the four electric field magnitudes, each detector measures one decay curve with the beam deflected toward it and one decay curve with the beam deflected away from it. One decay curve from each magnitude of electric field is shown in Fig. 22.

We took data by stepping the detectors both upstream and downstream to randomize any change in the hydrogenlike fraction in the beam or changes in the background. Each decay curve has at least fifteen thousand counts distributed among at least fourteen detector positions. The two thousand counts which comprise a typical data point are the sum of the counts in the 2.0-keV–2.5-keV (in the rest frame of the beam) portion of the two-photon spectra. The count rate was normalized to the integrated current obtained from stopping the beam in a Faraday cup. The data shown in Fig. 22 are corrected for changes in intensity due to beam trajectory effects, radiation anisotropy, and x-ray detector efficiency. Background has been subtracted but no correction is made for the presence of heliumlike argon spectra.

### 8. Background

A schematic diagram of the apparatus used to measure the lifetime of the quenched  $2^2S_{1/2}$  state of hydrogenlike argon is shown in Fig. 17. This apparatus differs from the apparatus in Fig. 3 used to measure the unperturbed  $2^2S_{1/2}$  state lifetime by the addition of a magnetic field and different Faraday cups. Our requirement that the experiment be performed with different magnetic fields and opposite field polarities, and consequently different beam trajectories, imposed restrictions on the type of the Faraday cup used. Two Faraday cups, one for each magnet polarity, were used. Each was a 0.5-m-long aluminum channel 5 cm deep. An unfortunate consequence of this

design is that it places the Faraday cup close to the x-ray detector, increasing both the background and the dead time. To reduce the flux of photons and charged particles from the Faraday cup reaching the nearby detector, we placed a 5-cm-thick curtain of lead bricks between each Faraday cup and the nearest x-ray detector. This is shown in Fig. 17.

The proximity of the Faraday cup to the x-ray detectors and the smaller number of decays in the two-photon portion of the quench spectra result in a much larger ratio of background to signal than in the decay of the unperturbed  $2^2S_{1/2}$  state. Because the geometry of the x-ray detectors and Faraday cups changes as the x-ray detectors move along the beam line, and because the background is more than a few percent of the count rate, we perform a separate background measurement at each detector position. The background is measured by recording a spectrum with the foil 75 cm upstream from its usual position in the magnet. The background count rate is obtained by summing the counts in the same energy region as used to obtain the quenched  $2^2S_{1/2}$  count rate and normalizing to the integrated beam current. The background is measured at every x-ray detector position for every magnetic field used in the experiment so that each quenched  $2^2S_{1/2}$  spectrum has a corresponding background spectrum. Moving the foil upstream has little effect upon the beam trajectory because ninety percent of the  $\text{Ar}^{18+}$  does not change charge states in the foil. Most of the remaining ions change from  $18+$  to  $17+$  which changes their deflection in the fringing field by about 6%, but their overall deflection by only a few percent.

When the foil is 75 cm upstream, about 0.5% of the initial  $2^2S_{1/2}$  population will reach the measurement region. The decay of the remaining 0.5% of the initial  $2^2S_{1/2}$  state population will give the appearance of a small position-dependent component in the background. Subtracting the counts from the quenched decay of the residual  $2^2S_{1/2}$  state along with the background does not change the measured lifetime of the quenched  $2^2S_{1/2}$  state.

We found the background either to be constant or to de-

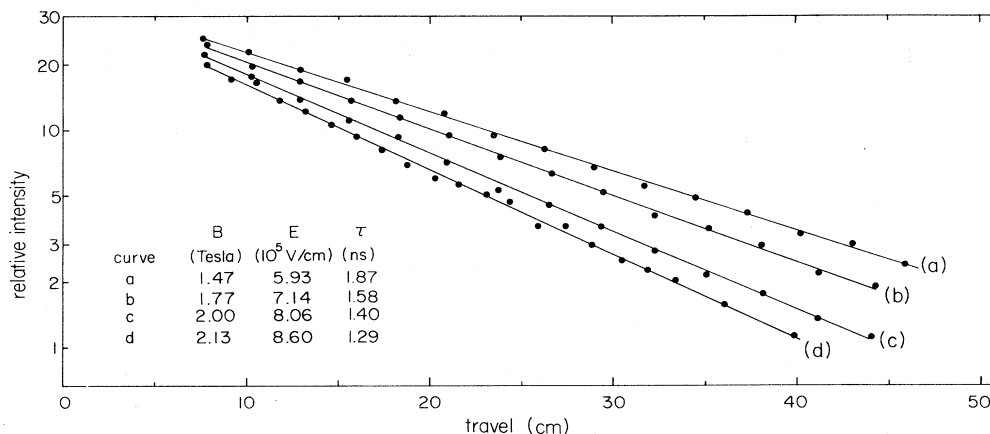


FIG. 22. Decay curves of the quenched  $2^2S_{1/2}$  state of hydrogenlike argon. The raw data are the spectra shown in Figs. 21(a)–21(d) and other spectra. A typical quenched  $2^2S_{1/2}$  decay curve extends 2.5 mean lives.

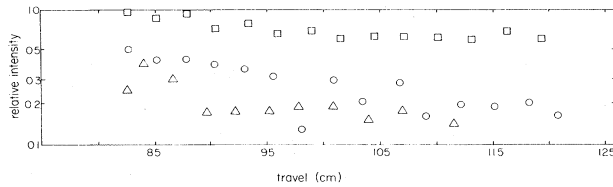


FIG. 23. Background as a function of beam travel downstream from the foil. (The foil has been moved 75 cm upstream.) The circles are the background from the beam in a 1.4-T field deflected away from the north detector; the triangles are the background from the beam in a 2.1-T field deflected toward the north detector; and the squares are the background from the beam in a 2.0-T field deflected away from the south detector. The scale in Fig. 23 is in the same units as the scale in Fig. 22. The background points represent between 30 and 100 counts, depending upon the background count rate.

crease as the x-ray detectors moved downstream. The background was  $2.0(+2.0, -1.0)\%$  of the quenched  $2^2S_{1/2}$  count rate when the x-ray detector was 5 cm downstream from the original foil position and  $10(+10, -5)\%$  of the quenched  $2^2S_{1/2}$  count rate when the x-ray detector was 20 cm downstream from the original foil position. The decay curves with the largest background exhibited the smallest position dependence. As in our measurement of the lifetime of the unperturbed  $2^2S_{1/2}$  state, the background in the south detector averages about 50% larger than the background in the north detector. Figure 23 shows the background count rate, as a function of x-ray detector position, from a beam bent toward the N detector in a field of 2.1 T, which had a very low background; a beam bent away from the N detector in a field of 1.4 T, which had a slightly higher background; and a beam bent away from the S detector in a field of 2.0 T, which has the highest background which we observed. We observed no correlation between the background and field strength or direction in which the beam was bent.

### 9. Dead time

In addition to high-energy photons and charged particles, large numbers of neutrons are produced by the 8.5-MeV/nucleon argon beam striking the Faraday cup and collimators. Scattering of a very-high-energy neutron in

the active portion of the x-ray detector deposits several hundred keV of energy in the detector. The time required for the x-ray detector electronics to recover from these high-energy events is usually the largest contribution to the detector dead time in this experiment. (See, for example, section IIB 14.) The lead shielding between the Faraday cup and the x-ray detectors is much less effective against fast neutrons than against charged particles and photons. Consequently, the behavior of the dead time in the two detectors was different. In both x-ray detectors the ratio of the x-ray detector dead time to x-ray count rate increased as the x-ray detector moved towards the Faraday cup. The effect was much larger in the detector towards which the beam was bent.

We also observed a peak in the dead time in the x-ray detector towards which the beam was deflected. The center of the dead-time peak was observed when the x-ray detector was 5 cm upstream from the center of the magnetic field, and the peak was about 3 cm wide. This additional dead time is caused by argon ions, whose energy is degraded in collisions with the edges of slits and are then deflected by the magnetic field and striking the x-ray detector window. The trajectory of a particle exiting the magnetic field after a total deflection of ninety degrees fixes its position at 5 cm upstream from the center of the magnet. A single ion, with an energy of 50 MeV or more, would produce a dead time of one hundred milliseconds. We greatly reduced the beam scattering and the dead-time peak by substituting hemispherical shaped jaws for the knife-edge jaws in our collimating slits.

The count rate was set by adjusting the beam intensity at the accelerator ion source so that the average dead time in the two detectors was about three percent. The decay of the  $2^2S_{1/2}$  state makes the contribution to the dead time from the x-ray count rate decrease in both detectors as a function of distance downstream from the foil. In the detector towards which the beam is deflected, the increase in neutron-induced dead time dominates and the overall dead time rises as the Faraday cup is approached.

### 10. Determination of the Lamb shift from the quenched $2^2S_{1/2}$ lifetime

After correction for beam trajectory effects (sections III C 2–5), and subtracting the background and the initial

TABLE III. Experimental Lamb-shift values (in THz) for different magnetic fields and detectors.

$B$ (T)	$E$ ( $10^5$ V/cm)	Deflection			
		Towards		Away	
		N Det.	S Det.	N Det.	S Det.
+ 1.77	+ 7.14	36.99			
- 1.77	- 7.14		39.85	40.01	
- 2.00	- 8.06		39.68	38.54	
+ 2.00	+ 8.06	38.73			37.54
- 2.13	- 8.60		38.26	38.80	
+ 2.13	+ 8.60	37.83			38.39
+ 1.47	+ 5.93	35.51			37.23
- 1.47	- 5.93		36.83	38.11	

3.5% heliumlike  $2^1S_0$  (section IIB 12), we fitted a single exponential to the decay curves. The resulting decay lengths were divided by the beam velocity determined by measurements of the total beam energy (section IIB 13) and corrected for time dilation (0.9%). In the electric fields of (5.93, 7.14, 8.06, and 8.60)  $\times 10^5$  V/cm we obtain quenched  $2^2S_{1/2}$  lifetimes of 1.87(0.03), 1.58(0.05), 1.40(0.02), and 1.28(0.02) ns, respectively. The errors here are the standard deviation of the mean of four lifetimes combined with a contribution averaging 0.01 ns for the uncertainty in the heliumlike  $2^1S_0$  contamination. Uncertainties in the beam velocity, dead time, and cascade effects increase the error by 0.3% of the mean life. The small corrections for dead time, cascades, etc., are omitted here.

The sixteen values of the hydrogenlike argon Lamb shift shown in Table III are determined from the sixteen lifetimes using Eqs. (3)–(5). The unweighted mean value of the sixteen Lamb-shift determinations is 37.99 THz with a standard deviation of 1.35 THz. The mean value weighted by one over the square of the standard deviation of the least-squares fits to the decay curves is 38.1 THz. Nine values lie above the mean value and seven below. The median value is 38.2 THz. A  $\chi^2$  test gives a value of  $\chi^2=1.0$  per degree of freedom, which is consistent with the 16 Lamb-shift values having a normal distribution with a mean of 38.0 THz and standard deviation of 1.35 THz.

For the electric fields of (5.93, 7.14, 8.06, and 8.60)  $\times 10^5$  V/cm the Lamb-shift values are 38.3(0.4), 38.6(0.9), 38.1(2.1), and 36.9(1.1) THz, respectively, where the values in parentheses are the standard deviations. Sorting the data by beam deflection we find that in experiments in which the beam is deflected towards the detector the Lamb shift is 37.96(1.49) THz, and in experiments in which the beam is deflected away from the x-ray detector the Lamb shift is 38.03(1.30) THz. The agreement of these two subsets of the data is additional evidence that our corrections for beam trajectory effects are accurate and complete. Subsets of the data grouped by detector and by chronology also show no differences. A grouping by magnet polarity, however, shows a difference of 1.5 THz [ 37.2(1.2) THz and 38.8 (1.1) THz] with six of the eight Lamb-shift values being higher for one of the polarities. We know of no effect which depends upon the polarity of the magnetic or electric field which does not also depend upon the direction of observation. There is no directional effect observable in our data, and we take this effect to be a statistical artifact.

### 11. Effect of cascades on the measured Lamb shift

Because the electric field can change the decay rates by mixing states of opposite parity, we consider whether electric field mixing of the high- $n, l$  states increases the cascade rate to the  $2^2S_{1/2}$  state. (Field free cascades were discussed in sections IIB 7–10.) For small electric fields, the mixing of states of opposite parity is of order  $(E\langle e\cdot r\rangle/W)^2$  where  $E$  is the electric field,  $\langle e\cdot r\rangle$ , the electric-dipole matrix element, and  $W$  the energy splitting. The electric-dipole matrix element scales roughly as  $n^2$ ,

and the fine-structure splitting as  $n^{-3}$ . For small electric fields the mixing of fine-structure states scales as  $n^{10}$  and the electric field splitting scales as  $n^7$ . This means that the electric field will mix the fine-structure states at relatively low  $n$ .

In the absence of an electric field the lower probability for electric-dipole transitions in which  $n$  and  $l$  change in the opposite sense makes the high- $nS$  states a relatively long-lived source of cascades to the  $2^2S_{1/2}$  states. The electric field mixes states of the same  $m_l$  belonging to different values of  $l$ . Since the  $nP$  states decay rapidly to the ground state the high- $nS$  states, as well as all other  $m_l=0$  and  $m_l=\pm 1$  states, are quenched. Similarly, the  $n, m_l=\pm 2$  states mix with the  $nD$  state, which has a much shorter lifetime than the high- $l$  states. The only unquenched states are the stretched states  $m_l=\pm(n-1)$ , which remains totally unquenched, and the high- $l, m_l$  states where the mixing does not appreciably change the decay rates. Because of the quenching of the low- $l$  states we expect less interference from cascades to the  $2^2S_{1/2}$  state in the measurement of the quenched  $2^2S_{1/2}$  lifetime.

When the interaction with the electric field is large compared to the fine-structure splitting, but still small compared to the Rydberg levels, the angular momentum states are replaced by a manifold of  $m_l^2$  levels. (In the limit of zero fine-structure splitting all of the levels belonging to the same  $m_l^2$  are degenerate.) In the strong-field case, the selection rule for radiative decay is  $\Delta m_l=0, \pm 1$ . The restriction that  $m_l$  change by at most 1 while  $n$  can decrease by any number consistent with the selection rule means that the decay of the  $n, m_l$  states follows a sequence similar to the  $n, l$  states in the field decay described in sections IIB 8 and IIB 9.

To obtain an experimental upper limit to the cascade rate into the  $2^2S_{1/2}$  state, we compare (as we did for the unperturbed  $2^2S_{1/2}$  state lifetime in section IIB 9) the count rates in our spectra from the  $n > 2 nP \rightarrow 1^2S_{1/2}$  Lyman series with the count rate of the two-photon continuum. We find the upper limit to the cascade rate to the  $2^2S_{1/2}$  state to be slightly lower than for the unperturbed  $2^2S_{1/2}$  lifetime.

### 12. The effect of a spectator electron on the Lamb shift

In section IIB 16, we considered the effect on the lifetime of the unperturbed  $2^2S_{1/2}$  state of a second (spectator) electron in a high- $n, l$  state. For the populations of doubly excited heliumlike ions likely to be present in the beam, we estimated that our measured  $2^2S_{1/2}$  lifetime would be 0.01% smaller than the actual  $2^2S_{1/2}$  lifetime. The same arguments hold for the electric field quenched lifetime of the  $2^2S_{1/2}$  state with the added consideration that many of the highly excited states are quenched before entering the measurement region.

In lifetime measurements the decay of the spectator electron results in a systematic error in the measurement. In a Lamb-shift measurement we also consider the perturbation of the  $2^2S_{1/2}$ - $2^2P_{1/2}$  energy splitting by the spectator electron. To see that the perturbation can be large although the change in the lifetime of the state is small, one need only consider that in heliumlike argon the  $2^1S_0$  state

has almost the same lifetime as the  $2^2S_{1/2}$  state while the  $2S$ - $2P$  splittings are typically 20 eV.

The interaction of an electron in the ground state with an electron in a high- $n$  state has been considered by Bethe and Salpeter<sup>79</sup> in connection with the polarization of excited states of helium. In the approximation that the outer electron is moving much slower than the inner electron, the outer electron may be treated as stationary relative to the inner electron. The electric field from the "stationary" outer electron is of order  $q/r_{1,2}^2$ , where  $q$  is the electron charge and  $r_{1,2}$  the distance between the two electrons. For  $r_{1,2}$  large compared to the Bohr radius of the inner electron, we approximate  $r_{1,2}$  by the Bohr radius of the outer electron:  $1/r \approx (Z-1)/a_0 n^2$ , where  $a_0$  is the Bohr radius in hydrogen. The electric field at the inner electron due to the "stationary" outer electron is then roughly  $1.5 \times 10^{12} n^{-4}$  (V/cm). The field from a  $n=18$  electron is in this approximation  $1.4 \times 10^7$  V/cm, which at twice the size of the quench field, does not produce a significant change in the  $2^2S_{1/2}$ - $2^2P_{1/2}$  splitting.

To examine the effect of the second electron on the  $2^2S_{1/2}$ - $2^2P_{1/2}$  splitting in greater detail we have used a Hartree-plus-statistical-exchange code<sup>80</sup> to calculate binding energies. In Table IV we list the change in the  $2^2S_{1/2}$ - $2^2P_{1/2}$  splitting as a function of the  $n, l$  state of a second electron. Table IV shows that perturbation of the second electron although quite significant for the  $nS$  states decreases rapidly with increasing  $n$  and especially with increasing  $l$ .

In the presence of the electric field, the  $nS$  states and any state of  $m_l=0$ , which can mix with the  $S$  state are quenched by mixing with the  $nP$ ,  $m_l=0$  state. The electric field leaves only a population of high- $m_l$  states whose perturbation on the  $n=2$  fine-structure is negligible. A second electron in a lower- $n$  state strongly perturbs the  $2^2S_{1/2}$ - $2^2P_{1/2}$  splitting, but the lifetimes and hence populations of these states are insignificant in our experiment.

### 13. Measurement errors

To account for error in the Lamb shift due to the systematic errors of cascades and dead time in the x-ray detectors we note that roughly half of the total  $2^2S_{1/2}$  decay rate is due to electric field quenching. In this situation the fractional error in the Lamb shift is the same as the fractional error in the quenched lifetime. The beam velocity enters into the determination of the Lamb shift both through the motional electric field and in determining the quenched lifetime from the measured decay length. Errors in the measurement of the beam velocity tend to

TABLE IV. Difference in binding energy (THz) of  $2s$  and  $2p$  electrons due to an electron in a high- $n, l$  state.

	Quantum numbers of the second electron						
	$l=0$	1	2	3	4	5	$>5$
$n=6$	52.3	38.8	35.2	11.2	3.3	1.3	
$n=12$	6.3	4.6	4.3	1.3	0.3	0	0
$n=18$	1.7	1.3	1.3	0.3	0	0	0

cancel in Eq. (3) and the contribution of errors in the velocity measurement to the error in the Lamb shift is about half the contribution to the  $2^2S_{1/2}$  state lifetime. Other corrections and errors in our Lamb-shift measurement are virtually the same as for our measurement of the unperturbed  $2^2S_{1/2}$  state lifetime, and are listed in Table V. The error due to contamination by the heliumlike  $2^1S_0$  state was computed by taking the differences between Lamb-shift values calculated with different percentages of heliumlike  $2^1S_0$  in the decay curve. Our final value for the Lamb shift in hydrogenlike argon is 37.89(0.38) THz.

### D. Comparison of results

Our experimental value of the Lamb shift in hydrogenlike argon is 37.89(0.38) THz. It is below, but in agreement with the theoretical Lamb-shift value of 38.250(0.025) THz obtained using Mohr's<sup>58,61,62</sup> calculation of the self-energy. Our experimental value, however, is not in agreement with the theoretical Lamb-shift value of 39.01(0.16) THz obtained using the self-energy calculation<sup>14,56</sup> by Erickson.

Since our first publication on this experiment,<sup>1</sup> six other measurements of the Lamb shift in the  $n=2$  state in the hydrogen isoelectronic sequence have been reported. Wood *et al.*<sup>59</sup> and Pellegrin, El Masri, Palffy, and Priells<sup>60</sup> have measured the Lamb shift by LASER resonance in hydrogenlike chlorine ( $Z=17$ ) and hydrogenlike phosphorus ( $Z=15$ ), respectively. Lundeen and Pipkin<sup>81</sup> and Newton, Andrews, and Unsworth<sup>82</sup> have measured the Lamb shift in hydrogen by double-loop rf resonance, and single-loop rf resonance, respectively, and Drake, Goldman, and van Wijngaarden,<sup>83</sup> and Curnutte, Cocke, and Dubois<sup>84</sup> have measured the Lamb shift in  $\text{He}^+$  and hydrogenlike oxygen ( $Z=8$ ) by the quench radiation anisotropy method. As with our experiment, each of these six experiments finds the Lamb shift to be smaller than the Lamb shift calculated using the self-energies of Mohr or Erickson. Five of the measurements also disagree with the Lamb shift calculated using Erickson's self-energy. The measurement of Lundeen and Pipkin<sup>80</sup> disagrees with the theoretical Lamb shift using Mohr's self-energy, but is in

TABLE V. Contributions to the measured Lamb shift.

Lamb shift (corrected for $2^1S_0$ )=37.99 THz	
Corrections (THz)	
collisional quenching	0.02
cascades	-0.04
dead time	-0.08
Errors (THz)	
collisional quenching	0.02
cascades	0.04
$2^1S_0$ fraction	0.14
beam velocity	0.04
dead time	0.08
measurement error	0.34
Hydrogenlike argon Lamb shift = 37.89(0.38) THz	

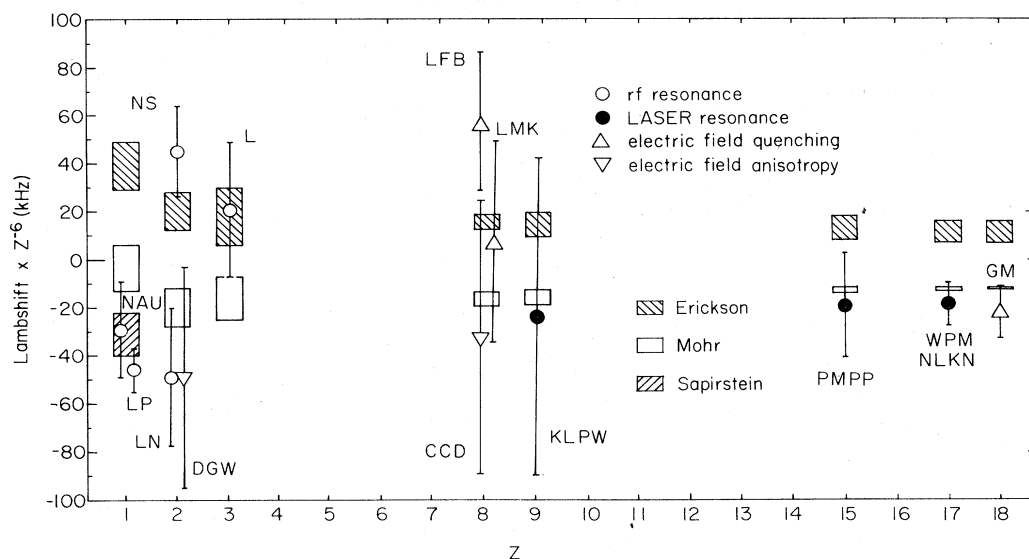


FIG. 24. Comparison of theory and experiments of the Lamb shift in the  $n=2$  state of the hydrogen isoelectronic sequence. Theory and experiment are plotted as a deviation from the average of the theoretical values. Experiments with uncertainties of less than  $100 \text{ kHz} \times Z^6$  are GM—this work, WPMNLKN—Ref. 59, PMPP—Ref. 60, KLPW—Ref. 85, CCD—Ref. 84, LFB—Ref. 86, LMK—Ref. 87, L—Ref. 88, NS—Ref. 89, LN—Ref. 90, DGW—Ref. 83, NAU—Ref. 82, and LP—Ref. 81.

agreement with theory when Sapirstein's<sup>56</sup> value for  $A_{60}$  [see Eq (2)] is used.

These experiments and earlier experiments<sup>85–90</sup> with errors small enough to potentially distinguish between the calculations of Erickson and Mohr are shown in Fig. 24. As in Fig 3. of Ref. 83, we have scaled the experimental and theoretical values by  $Z^6$  and plot the experimental and theoretical values as a deviation from the average of the theoretical values. The  $Z^6$  scaling shows the discrepancy between Lamb-shift values calculated by Erickson and Mohr which scale roughly as  $Z^6$ . The value of high  $Z$ -Lamb-shift measurements in distinguishing between the two calculations is apparent in Fig. 24.

#### ACKNOWLEDGMENTS

This experiment was made possible by the excellent and extensive support provided by the Lawrence Berkeley Laboratory. Over a period of seven years more than 50 people contributed to the design, fabrication, operation, and analysis of the experiments. Dr. Joseph Jaklevic, Mr. Donald Landis, Mr. Almon Larsh, Jr., Mr. Norman Madden, and Mr. Donald Malone designed the x-ray detectors, and designed and customized the electronics for the x-ray detectors, the dead-time correction system, and the beam-energy measurement. Mr. Jack Gunn, Dr. Klaus Halbach,

Mr. Terry Jackson, Mr. Steven Magyary, Mr. Donald Nelson, and Mr. Donald Yee designed the magnet, the magnet pole tips, the shims and magnet power supply, and supplied the equipment and instruction for measuring the magnetic fields. Mr. Richard Leres wrote the data-acquisition software. Mr. Warren Harnden assisted in the custom design of the vacuum chamber and mechanical hardware. Mr. Leon Archambault fabricated and mounted the foils, Mr. Ivor Woods and Mr. Walter Quan fabricated the masks for the Soller slits. Mr. Albert Ghorso was generous with his equipment, with his advice and assistance, and with his beam time. Professor Peter Mohr gave us theoretical guidance and patient explanations. The operators and staff of the 88-in. cyclotron produced a record energy beam for calibrating the surface barrier detectors. The operators and staff of the Super-HILAC routinely performed heroic deeds at all hours of the day and night. Their skill and dedication were the major factors in obtaining the very high quality beams necessary for precision experiments. We thank them all, but most especially we thank our engineer, Mr. Douglas MacDonald, who contributed to all aspects of the experiment. This work was supported by the Director, Office of Energy Research, Office of Basic Energy Sciences, Chemical Sciences Division of the U.S. Department of Energy, under Contract No. DE-AC03-76SF00098.

<sup>1</sup>H. Gould and R. Marrus, Phys. Rev. Lett. **41**, 1457 (1978).

<sup>2</sup>S. P. Goldman and G. W. F. Drake, Phys. Rev. A **24**, 183 (1981).

<sup>3</sup>W. R. Johnson, Phys. Rev. Lett. **29**, 1123 (1972).

<sup>4</sup>F. A. Parpia and W. R. Johnson, Phys. Rev. A **26**, 1142 (1982).

<sup>5</sup>See, for example, R. Marrus and P. J. Mohr, in *Advances in Atomic and Molecular Physics: Forbidden transitions in one- and two-electron atoms*, edited by D. R. Bates and B. Bederson (Academic, N.Y., 1978), Vol. 14, p. 181.

<sup>6</sup>M. Goeppert-Mayer, Naturwissenschaften **17**, 932 (1929); Ann.

- Phys. (Leipzig)[5] **9**, 273 (1931).
- <sup>7</sup>G. Breit and E. Teller, *Astrophys. J.* **91**, 215 (1940).
- <sup>8</sup>L. Spitzer, Jr. and J. L. Greenstein, *Astrophys. J.* **114**, 407 (1951); J. Shapirio and G. Breit, *Phys. Rev.* **113**, 179 (1959).
- <sup>9</sup>B. A. Zon and L. P. Rapaport, *Zh. Eksp. Teor. Fiz. Pis'ma Red.* **7**, 70 (1968) [*Sov. Phys. JETP Lett.* **7**, 52 (1968)].
- <sup>10</sup>S. Klarsfeld, *Phys. Lett.* **30A**, 382 (1969).
- <sup>11</sup>J. Sucher, in *Atomic Physics 5, Proceedings of the Fifth International Conference on Atomic Physics 1976*, edited by R. Marrus, M. Prior, and H. Shugart, (Plenum, N.Y., 1977), pp. 415–451.
- <sup>12</sup>D. L. Lin and G. Feinberg, *Phys. Rev. A* **10**, 1425 (1974); R. Barbieri and J. Sucher, *Nucl. Phys. B* **134**, 155 (1978).
- <sup>13</sup>C. K. Au, *Phys. Rev. A* **14**, 531 (1976).
- <sup>14</sup>G. W. Erickson, *J. Phys. Chem. Ref. Data* **6**, 831 (1977).
- <sup>15</sup>R. Marrus and R. W. Schmieder, *Phys. Rev. A* **5**, 1160 (1972).
- <sup>16</sup>G. W. F. Drake, G. A. Victor, and A. Dalgarno, *Phys. Rev.* **180**, 25 (1969).
- <sup>17</sup>C. D. Lin, W. R. Johnson, and A. Dalgarno, *Phys. Rev. A* **15**, 154 (1977).
- <sup>18</sup>A. Dalgarno, *The Menzel Symposium*, NBS Spec. Publ. No. 353 (U.S. GPO, Washington, D.C., 1971), p. 47. Values from this work are quoted in Ref. 17.
- <sup>19</sup>J. Alonso, D. Dietrich, and H. Gould, *IEEE Trans. Nucl. Sci.* **NS-26**, 3686 (1979); H. Gould (private communication); for experimental details see J. Alonso and H. Gould, *Phys. Rev. A* **26**, 1134 (1982) and references contained therein.
- <sup>20</sup>H. Gould, R. Marrus, and R. W. Schmieder, *Phys. Rev. Lett.* **31**, 504 (1973).
- <sup>21</sup>C. Schwartz (private communication); G. W. F. Drake, *Phys. Rev. A* **3**, 908 (1971); **5**, 1979 (1972); G. Feinberg and J. Sucher, *Phys. Rev. Lett.* **26**, 681 (1971); I. L. Beigman and U. I. Safronova, *Zh. Eksp. Teor. Fiz.* **60**, 2045 (1971) [*Sov. Phys. JETP* **33**, 1102 (1971)]; W. R. Johnson and C. P. Lin, *Phys. Rev. A* **9**, 1486 (1974); **14**, 565 (1976); S. A. Zapyrgaev, N. L. Manakov, and V. G. Palychikov, *Opt. Spektrosk.* **46**, 214 (1979) [*Opt. Spectrosc. (USSR)* **46**, 119 (1980)].
- <sup>22</sup>D. L. Matthews and R. J. Fortner, in *Beam Foil Spectroscopy*, edited by I. A. Sellin and D. J. Pegg, (Plenum, N.Y., 1975), Vol. 2, p. 545. A calculation of the collisional quenching rate in heliumlike fluorine is given by J. I. Gersten, *Phys. Rev. A* **15**, 940 (1977).
- <sup>23</sup>See, for example, F. S. Goulding and R. H. Pehl, in *Nuclear Spectroscopy and Reactions: Semiconductor radiation detectors*, edited by J. Cerny (Academic, N.Y., 1974), Part A, pp. 290–342; F. S. Goulding and D. A. Landis, *Semiconductor detector spectrometer electronics*, *ibid.*, pp. 414–481.
- <sup>24</sup>W. Soller, *Phys. Rev.* **24**, 158 (1924).
- <sup>25</sup>W. H. McMaster, N. Kerr Del Grande, J. H. Mallett, and J. H. Hubbell, *Compilation of X-Ray Cross Sections*, Lawrence Livermore Laboratory Report No. UCRL-50174, Sec. II, Rev. 1 (National Technical Information Service, U.S. Dept of Commerce, Springfield, VA 22151, 1969).
- <sup>26</sup>J. T. Routti and S. G. Prussin, *Nucl. Instrum. Methods* **72**, 125 (1969); J. T. Routti, *SAMPO, a FORTRAN IV Program for Computer Analysis of Gamma Spectra from Ge(Li) Detectors, and for Other Spectra With Peaks*, Lawrence Berkeley Laboratory Report No. UCRL-19452 (National Technical Information Service, U.S. Dept. Commerce, Springfield VA 22151, 1969). The most recent version of SAMPO is described by M. J. Koskelo, P. A. Aarnio, and J. Routti, *Comp. Phys. Commun.* **24**, 11 (1981).
- <sup>27</sup>Binding energies of the heliumlike  $n=2$  states are evaluated by means of the  $Z$  expansion of the nonrelativistic energies from R. E. Knight and C. W. Sherr, *Rev. Mod. Phys.* **35**, 431 (1963); together with the  $Z$  expansion of the lowest-order relativistic corrections from H. T. Doyle, in *Advances in Atomic and Molecular Physics: Relativistic Z-dependent corrections to atomic energy levels*, edited by D. R. Bates and I. Esterman (Academic, New York, 1969), Vol. 5, pp. 337–413.
- <sup>28</sup>H. Gould, R. Marrus, and P. J. Mohr, *Phys. Rev. Lett.* **33**, 676 (1974); G. W. F. Drake, *Astrophys. J.* **158**, 1199 (1969).
- <sup>29</sup>W. A. Davis and R. Marrus, *Phys. Rev. A* **15**, 1963 (1977).
- <sup>30</sup>W. J. Braithwaite, D. L. Matthews, and C. F. Moore, *Phys. Rev. A* **11**, 465 (1975).
- <sup>31</sup>W. Nitsche, E. Trabert, and P. H. Heckmann, *J. Phys. (Paris) Colloq.* **40**, C1-266 (1979).
- <sup>32</sup>P. Richard, *Phys. Lett.* **45A**, 13 (1973).
- <sup>33</sup>H. Homma, R. R. Lewis, and R. T. Robiscoe, *Phys. Rev. A* **25**, 333 (1982); H.-D. Betz, J. Rothermel, and F. Bell, *Nucl. Instrum. Methods* **170**, 243 (1980); R. W. Hasse, H.-D. Betz, and F. Bell, *J. Phys. B* **12**, L711 (1979); F. Hopkins and P. von Brentano, *ibid.* **9**, 775 (1976); F. Hopkins, J. Sokolov, and P. von Brentano, in *Beam Foil Spectroscopy*, edited by I. A. Sellin and D. J. Pegg (Plenum, N.Y., 1975), Vol. 2, p. 553.
- <sup>34</sup>Nonrelativistic transition probabilities were calculated from the formulas in H. A. Bethe and E. E. Salpeter, *Quantum Mechanics of One- and Two-Electron Atoms* (Springer-Verlag, Berlin, 1957), Chap. 4.
- <sup>35</sup>R. Marrus and R. W. Schmieder, *Phys. Rev. Lett.* **25**, 1689 (1970).
- <sup>36</sup>R. Marrus and R. W. Schmieder (private communication).
- <sup>37</sup>R. W. Schmieder and R. Marrus, *Phys. Rev. Lett.* **25**, 1692 (1970).
- <sup>38</sup>R. M. Main, *Nucl. Instrum. Methods* **97**, 51 (1971).
- <sup>39</sup>See, for example, J. B. Moulton, J. E. Stephenson, R. P. Schmitt, and G. J. Wozniak, *Nucl. Instrum. Methods* **157**, 325 (1978), and references contained therein. This paper describes an energy measurement similar to ours.
- <sup>40</sup>R. E. Hintz, F. B. Selph, W. S. Flood, B. G. Harvey, F. G. Resmini, and E. A. McClatchie, *Nucl. Instrum. Methods* **72**, 61 (1969).
- <sup>41</sup>L. C. Northcliffe and R. F. Schilling, *Nucl. Data Tables* **7**, 324 (1970).
- <sup>42</sup>*Table of Isotopes*, 7th ed., edited by C. M. Lederer and V. S. Shirley (Wiley, N.Y., 1978), pp. 1360, 1361.
- <sup>43</sup>R. H. Pehl, F. S. Goulding, D. A. Landis, and M. Lenzlinger, *Nucl. Instrum. Methods* **59**, 45 (1968).
- <sup>44</sup>R. W. Schmieder and R. Marrus, *Phys. Rev. Lett.* **25**, 1245 (1970); H. Gould, R. Marrus, and R. W. Schmieder, *ibid.* **31**, 504 (1973); H. Gould and R. Marrus, *Bull. Am. Phys. Soc.* **21**, 84 (1976).
- <sup>45</sup>C. L. Cocke, B. Curnutte, and R. Randall, *Phys. Rev. Lett.*, **31**, 507 (1973).
- <sup>46</sup>J. A. Bednar, C. L. Cocke, B. Curnutte, and R. Randall, *Phys. Rev. A* **11**, 460 (1975).
- <sup>47</sup>D. L. Lin and L. W. Armstrong Jr., *Phys. Rev. A* **16**, 791 (1977); A. Ghiorso (private communication).
- <sup>48</sup>C. L. Cocke, B. Curnutte, J. R. Macdonald, J. A. Bednar, and R. Marrus, *Phys. Rev. A* **9**, 2242 (1974).
- <sup>49</sup>Ph. Deschepper, P. Lebrun, L. Palffy, and P. Pellegrin, *Phys. Rev. A* **24**, 1633 (1981).
- <sup>50</sup>E. A. Hinds, J. E. Clendenin, and R. Novick, *Phys. Rev. A* **17**, 670 (1978).
- <sup>51</sup>M. H. Prior, *Phys. Rev. Lett.* **29**, 611 (1972).
- <sup>52</sup>C. A. Kocher, J. E. Clendenin, and R. Novick, *Phys. Rev. Lett.* **29**, 615 (1972).

- <sup>53</sup>S. J. Brodsky and P. J. Mohr, in *Topics in Current Physics: Quantum Electrodynamics in Strong and Supercritical Fields*, edited by I. A. Sellin (Springer, Berlin, 1978), Vol. 5, p.3.
- <sup>54</sup>H. A. Bethe, Phys. Rev. 72, 339 (1947); H. A. Bethe, L. M. Brown, and J. R. Stehn, *ibid.* 77, 370 (1950); J. M. Harriman, *ibid.* 101, 594 (1956); C. Schwartz and J. J. Tiemann, Ann. Phys. (N.Y.) 6, 178 (1959); M. Lieber, Phys. Rev. 174, 2037 (1968); R. W. Huff, *ibid.* 186, 1367 (1969); S. Klarsfeld and A. Marquet, Phys. Lett. 43B, 201 (1973); R. P. Feynman, Phys. Rev. 74, 1430 (1948); 76, 769 (1949); H. Fukuda, Y. Miyamoto, and S. Tomonaga, Prog. Theor. Phys. (Kyoto) 4, 47,121 (1949); N. M. Kroll and W. E. Lamb, Jr., Phys. Rev. 75, 388 (1949); J. Schwinger, *ibid.* 75, 898 (1949); J. B. French and V. F. Weisskopf, *ibid.* 75, 1240 (1949); M. Baranger, *ibid.* 84, 866 (1951); R. Karplus, A. Klein, and J. Schwinger, *ibid.* 86, 288 (1952); M. Baranger, H. A. Bethe, and R. P. Feynmann, *ibid.* 92, 482 (1953); A. J. Layzer, Phys. Rev. Lett. 4, 580 (1960); A. J. Layzer, J. Math. Phys. 2, 292, 302 (1961); H. M. Fried and D. R. Yennie, Phys. Rev. Lett. 4, 583 (1960); Phys. Rev. 112, 1391 (1958).
- <sup>55</sup>G. W. Erickson, and D. R. Yennie, Ann. Phys. (N.Y.) 35, 271, 447 (1965).
- <sup>56</sup>G. W. Erickson, Phys. Rev. Lett. 27, 780 (1971).
- <sup>57</sup>J. Sapirstein, Phys. Rev. Lett. 47, 1723 (1981).
- <sup>58</sup>P. J. Mohr, Ann. Phys. (N.Y.) 88, 26 (1974).
- <sup>59</sup>O. R. Wood II, C. K. N. Patel, D. E. Murnick, E. T. Nelson, M. Leventhal, H. W. Kugel, and Y. Niv, Phys. Rev. Lett. 48, 398 (1982).
- <sup>60</sup>P. Pellegrin, Y. El Masri, L. Palffy, and R. Priells, Phys. Rev. Lett. 42, 1762 (1982).
- <sup>61</sup>P. J. Mohr, Phys. Rev. A 26, 2338 (1982); Phys. Rev. Lett. 34, 1050 (1975); Ann. Phys. (N.Y.) 88, 52 (1974).
- <sup>62</sup>P. J. Mohr, in *Beam Foil Spectroscopy*, edited by I. A. Sellin and D. J. Pegg, (Plenum, New York, 1975), Vol. 1, p.89.
- <sup>63</sup>R. Serber, Phys. Rev. 48, 49 (1935); E. A. Uehling, *ibid.* 48, 55 (1935); E. H. Wichmann and N. M. Kroll, *ibid.* 101, 843 (1956).
- <sup>64</sup>See, for example, B. E. Lautrup, A. Peterman, and E. de Rafael, Phys. Rep. 3, 193 (1972). This article gives references to the original work.
- <sup>65</sup>V. Rojansky and J. H. Van Vleck, Phys. Rev. 32, 327 (1928).
- <sup>66</sup>M. Hillery and P. J. Mohr, Phys. Rev. A 21, 24 (1980).
- <sup>67</sup>W. E. Lamb, Jr. and R. C. Retherford, Phys. Rev. 79, 549 (1950).
- <sup>68</sup>G. W. F. Drake and R. B. Grimley, Phys. Rev. A 8, 157 (1973).
- <sup>69</sup>P. J. Mohr, Phys. Rev. Lett. 40, 854 (1978).
- <sup>70</sup>A. van Wijngaarden and G. W. F. Drake, Phys. Rev. A 25, 400 (1982); A. van Wijngaarden, R. Helbing, J. Patel, and G. W. F. Drake, *ibid.* 25, 862 (1982).
- <sup>71</sup>P. G. Watson and R. F. DiGregorio, in *Proceedings of the International Symposium on Magnetic Technology, Stanford, 1956* (National Bureau Standards, U.S. Dept. Commerce, Springfield, VA, 1965), p.393 [University of California Radiation Laboratory Report No. UCRL 16357 (unpublished)].
- <sup>72</sup>H. A. Wheller, Proc. IRE 16, 1398 (1928); W. F. Brown and J. H. Sweer, Rev. Sci. Instrum. 16, 276 (1945); K. J. Williamson, J. Sci. Instrum. 24, 242 (1947); R. F. K. Herzog and O. Tischler, Rev. Sci. Instrum. 24, 1001 (1953); C. G. Doles and P. G. Watson, University of California Radiation Laboratory Engineering Note UCID-1602-2 (revised 1969) (unpublished).
- <sup>73</sup>F. W. Macondray, in *Proceedings of the Second International Symposium on Magnet Technology, Oxford, July 11–14, 1967* (Rutherford Laboratory, Chilton, England), p.639 [University of California Radiation Laboratory Report No. UCRL 17639 (unpublished)].
- <sup>74</sup>K. Halbach and S. Magyary (private communication); K. Halbach, in *Proceedings of the Second International Symposium on Magnet Technology, Oxford, July 11–14, 1967* (Rutherford Laboratory, Chilton, England), p.47 [University of California Radiation Laboratory Report No. UCRL 17436 (unpublished)].
- <sup>75</sup>V. F. Weisskopf, Phys. Today 13, (9), 24 (1960); see also J. Terrell, Phys. Rev. 116, 1041 (1959).
- <sup>76</sup>R. H. Pehl and J. T. Walton (private communication).
- <sup>77</sup>H. Kanter and E. J. Sternglass, Phys. Rev. 126, 620 (1962).
- <sup>78</sup>R. Woldseth, *All You Ever Wanted to Know About X-Ray Energy Spectrometry* (Kevex Corp., Burlingame, 1973), pp. 2.11, 2.12.
- <sup>79</sup>H. A. Bethe and E. E. Salpeter, *Quantum Mechanics of One- and Two-Electron Atoms* (Springer-Verlag, Berlin, 1957), pp. 137–139.
- <sup>80</sup>R. D. Cowan, Phys. Rev. 163, 54 (1967); R. D. Cowan and D. C. Griffin, J. Opt. Soc. Am. 66, 1010 (1976).
- <sup>81</sup>S. R. Lundeen and F. M. Pipkin, Phys. Rev. Lett. 46, 232 (1981).
- <sup>82</sup>G. Newton, D. A. Andrews, and P. J. Unsworth, Philos. Trans. R. Soc. London 290, 373 (1979).
- <sup>83</sup>G. W. F. Drake, S. P. Goldman, and A. van Wijngaarden, Phys. Rev. A 20, 1299 (1979).
- <sup>84</sup>B. Curnutte, C. L. Cocke, and R. D. Dubois, Nucl. Instrum. Methods 202, 119 (1982).
- <sup>85</sup>H. W. Kugel, M. Leventhal, C. K. N. Patel, and O. R. Wood II, Phys. Rev. Lett. 35, 647 (1975).
- <sup>86</sup>G. P. Lawrence, C. Y. Fan, and S. Bashkin, Phys. Rev. Lett. 28, 1612 (1972); 29, 320 (1972).
- <sup>87</sup>M. Leventhal, D. E. Murnick, and H. W. Kugel, Phys. Rev. Lett. 28, 1609 (1972).
- <sup>88</sup>M. Leventhal, Phys. Rev. A 11, 427 (1975).
- <sup>89</sup>M. A. Narasimham and R. L. Strombotne, Phys. Rev. A 4, 14 (1971).
- <sup>90</sup>E. Lipworth and R. Novick, Phys. Rev. 108, 1434 (1957).